Low-voltage SEM of air-sensitive powders: from sample preparation to micro/nano analysis with secondary electron hyperspectral imaging.

Article:

Nohl, J.F., Farr, N.T.H. orcid.org/0000-0001-6761-3600, Sun, Y. et al. (3 more authors) (2022) Low-voltage SEM of air-sensitive powders: from sample preparation to micro/nano analysis with secondary electron hyperspectral imaging. Micron, 156. 103234. ISSN 0968-4328

https://doi.org/10.1016/j.micron.2022.103234

Micron 156 (2022) 103234

Contents lists available at ScienceDirect

Micron

journal homepage: www.elsevier.com/locate/micron

Low-voltage SEM of air-sensitive powders: From sample preparation to micro/nano analysis with secondary electron hyperspectral imaging

James F. Nohl[a,b,*], Nicholas T.H. Farr[a,c], Yige Sun[b,d], Gareth M. Hughes[e], Serena A. Cussen[a,b,f], Cornelia Rodenburg[a]

[a] Department of Materials Science and Engineering, The University of Sheffield, Mappin Street, Sheffield S1 3JD, UK
[b] The Faraday Institution, Quad One, Becquerel Avenue, Harwell Campus, Didcot OX11 0RA, UK
[c] Insigneo Institute for In Silico Medicine, The University of Sheffield, Pam Liversidge Building, Sir Robert Hadfield Building, Mappin Street, S1 3JD, UK
[d] Department of Materials, University of Oxford, Parks Road, Oxford OX1 3PH, UK
[e] David Cockayne Centre for Electron Microscopy, Department of Materials, Parks Rd, Oxford OX1 3PH, UK
[f] Department of Biological and Chemical Engineering, The University of Sheffield, Mappin Street, Sheffield S1 3JD, UK

ARTICLE INFO

Keywords:
Low-voltage scanning electron microscopy (LV-SEM)
Secondary electron hyperspectral imaging (SEHI)
Powder characterization
Energy storage materials
Additive manufacturing (AM) materials

ABSTRACT

Powder materials are used in all corners of materials science, from additive manufacturing to energy storage. Scanning electron microscopy (SEM) has developed to meet morphological, microstructural and bulk chemical powder characterization requirements. These include nanoscale elemental analysis and high-throughput morphological assays. However, spatially localized powder surface chemical information with similar resolution to secondary electron (SE) imaging is not currently available in the SEM. Recently, energy filtered (EF-) SEM has been used for surface chemical characterization by secondary electron hyperspectral imaging (SEHI). This review provides a background to existing powder characterization capabilities in the low voltage SEM provided by SE imaging, EDX analysis and BSE imaging and sets out how these capabilities could be extended for surface chemical analysis by applying SEHI to powders, with particular emphasis on air and beam sensitive powder surfaces. Information accessible by SEHI, its advantages and limitations, is set into the context of other chemical characterization methods that are commonly used for assessing powder surface chemistry such as by Auger electron spectroscopy (AES) and X-ray photoelectron spectroscopy (XPS). The applicability of existing powder preparation methods for SEM to SEHI is also reviewed. An alternative preparation method is presented alongside first examples of SEHI characterization of powder surfaces. The commercial powder materials used as examples were carbon-fiber/polyamide composite powder feedstock (CarbonMide®) used in additive manufacturing and powders consisting of lithium nickel cobalt oxide (NMC). SEHI is shown to differentiate bonding present at carbonaceous material surfaces and extract information about the work function of metal oxide surfaces. The surface sensitivity of SEHI is indicated by comparison of pristine powders to those with surface material added in

---

Abbreviations: AE, Auger electron; AES, Auger electron spectroscopy; AM, Additive manufacturing; AV, Accelerating voltage; BD, Beam deceleration; BSE, Backscatter electron; CB, Carbon black; CD, Critical dimension; CF, Carbon fiber; CM, CarbonMide®; CT, Computerized tomography; DOS, Density of states; EBID, Electron beam induced deposition; EDX, Energy dispersive X-ray; EF, Energy filtered; E_L, Landing energy, energy at which PEs interact with the specimen; EOS, Electro Optical Systems; ETD, Everhart-Thornley detector; FIB, Focussed ion beam; FOV, Field of view; HeIM, Helium ion microscope; HFW, Horizontal field width; HOPG, Highly oriented pyrolytic graphite; HV, High-voltage; I_0, Incident beam current; IMFP, Inelastic mean free path, mean distance the SE travels between inelastic collisions; KPAFM, Kelvin probe atomic force microscopy; LIB, Lithium-ion battery; LV, Low-voltage; MAI, Methylamonium iodide; MAPbI3, Methylamonium lead iodide; MAST-SEY, MAterial Simulation Toolkit for Secondary Electron Yield; MED, Mean escape depth, average depth from the surface that SEs are emitted from; MV, Mirror Voltage; NMC, Nickel manganese cobalt oxide; NMP, N-methyl pyrrolidone; NRMSD, Normalized root mean square deviation; OPV, Organic photovoltaic; P3HT, poly(3-hexylthiophene); PA, Polyamide; PE, Primary electron, electron in the incident electron beam; PFIB, Plasma focussed ion beam; PVDF, Polyvinylidene fluoride; ROI, Region of interest; SAM, Scanning Auger microscope; SD, Standard deviation; SDD, Silicon drift detector; SE, Secondary electron; SE1, SE emissions localized to the PE interaction from which UHR SE images are formed; SE2, SE emissions delocalized in time and space from the PE interaction; SEHI, Secondary electron hyperspectral imaging; SEM, Scanning electron microscope/microscopy; SLS, Selective laser sintering; STEM, Scanning transmission electron microscope; SEY, Secondary electron yield, the ratio of emitted SEs to PEs; TEM, Transmission electron microscope; TLD, Through-lens detector; UC, UniColore; UHR, Ultra-high resolution; UHV, Ultra-high vacuum; WD, Working distance, distance between where the electron beam is focussed and the pole piece; XPS, X-ray photoelectron spectroscopy; φ, Work function, minimum energy required to remove an electron from a metal surface.

* Corresponding author at: Department of Materials Science and Engineering, The University of Sheffield, Mappin Street, Sheffield S1 3JD, UK.
E-mail address: jnohl1@sheffield.ac.uk (J.F. Nohl).

https://doi.org/10.1016/j.micron.2022.103234
Received 7 December 2021; Received in revised form 2 March 2022; Accepted 2 March 2022

preparation. A minimum spatial localization of chemical information of 55 nm was achieved in differentiating regions of NMC surface chemistry by distinct SE spectra.

1. Introduction

Products ranging from batteries, pharmaceuticals and foods are made from powder feed stocks. In addition, powder-based additive manufacturing (AM) uses powder feedstocks to form 3D parts in the medical, automotive and aerospace sectors. Advances in these areas depends on reliably controlling powder properties, including powder morphology, chemistry (bulk and surface) and microstructure.

Characterization of powders is a fundamental component in advancing powder properties. The scanning electron microscope (SEM) is already widely used for characterization of powder morphology and microstructure, as well as for bulk chemical information (Galvão et al., 2018). Attributes of morphology and microstructure characterized by SEM include size, shape, surface texture, bulk chemistry and even crystal structure. When the SEM is combined with a focused ion beam (FIB) the internal porosity can also be determined (Walde et al., 2018). However, characterization of surface chemistry on the sub-micron length scale of particle surface features such as those shown in Figs. 1a and 1b are not currently routinely accessible in the SEM/FIB-SEM. Currently, the surface chemistry of powders is often assessed by spectroscopic methods such as X-ray photoelectron spectroscopy (XPS), see example in Fig. 1c, or Auger electron spectroscopy (AES). These methods do not provide the high spatial resolution SE imaging in the low voltage SEM (LV-SEM) can achieve.

This disconnect in the spatial localization of information might be addressed if secondary electron hyperspectral imaging (SEHI) proves feasible for the surface chemical analysis of powders. SEHI is a method of detecting secondary electrons (SEs) with energy and spatial information in the LV-SEM. One implementation of this is to serially collect SE images with a predetermined cut-off energy per image to create a SEHI data volume (Fig. 2a). The energy-dimension of the data volume can be used to derive SE energy spectra (as explained in Section 5.4) (Nohl, 2020; Stehling et al., 2018). In Fig. 2a, SE emissions from powder surfaces contain chemical contrast. The low energy SE spectra (Fig. 2b) can provide spatially localized chemical information and qualitative comparison of surface chemistry at the nanoscale, for example between square regions with 100 nm side length outlined Fig. 2a. The regions of the spectra in Fig. 2b labeled sp^2, NMC and CHx denote sp^2-like carbon, lithium nickel manganese cobalt oxide and amorphous hydrogenated carbon surface chemistries. Attribution of these energy regions is described in Sections 5.5.1 and 5.5.2 with test powder materials from additive manufacturing material and LIB cathode material respectively.

Powder surface chemistry variation at these length scales is of interest to the development of novel powder feedstocks. The surface properties can determine usefulness of powder materials, such as the shelf life of food powders (Burgain et al., 2017) and the cycle-life of lithium-ion batteries (LIBs) (Lim et al., 2020). The use of a single instrument with access to surface chemical variation on powder surfaces could provide significant advantage in gaining direct insights into the mechanisms involved in surface chemical modification/stabilization in relation to any performance difference. However, at present these insights into surface morphology and chemistry are provided by multiple techniques, often with a disconnect in the spatial localization of information. For example, Lim et al. use a combination of X-ray photoelectron spectroscopy (XPS) and transmission electron microscopy (TEM) to measure the average surface chemistry of the LIB cathode and local graphite surface treatment of individual nanoparticles (Lim et al., 2020). This was necessary due to the spatially averaging nature of XPS (Galvão et al., 2018) and high-resolution imaging of individual particles provided by electron microscopy.

Similarly in AM, the properties of fabricated parts are dependent on powder surface chemistry. Metallic powder particle surfaces react with air to form oxide layers which increase microstructural pore formation during manufacture (Ernst et al., 2020; Leung et al., 2019). Likewise, surface oxidation of polymer powder feedstocks can occur and affect the molecular weight. The mechanical properties of the resulting parts are affected by pore structures formed (Salehi and Pircheraghi, 2021), with size and position of pores being major contributors to the number of cycles to failure that a part can withstand (Tammas-Williams et al., 2017).

Given that SEM is already routinely used to characterize morphological, microstructural and bulk chemical properties of powder materials, the addition of nanoscale surface chemical characterization in the SEM represents a significant increase in capability for powder characterization. Recent developments in detectors for LV-SEM energy dispersive X-ray (EDX) (LV-EDX) analysis (see Sections 2.1 and 2.2) have made surface elemental characterization of metallic nanoparticles in the SEM possible (Burgess et al., 2017; Asahina et al., 2012). Despite these

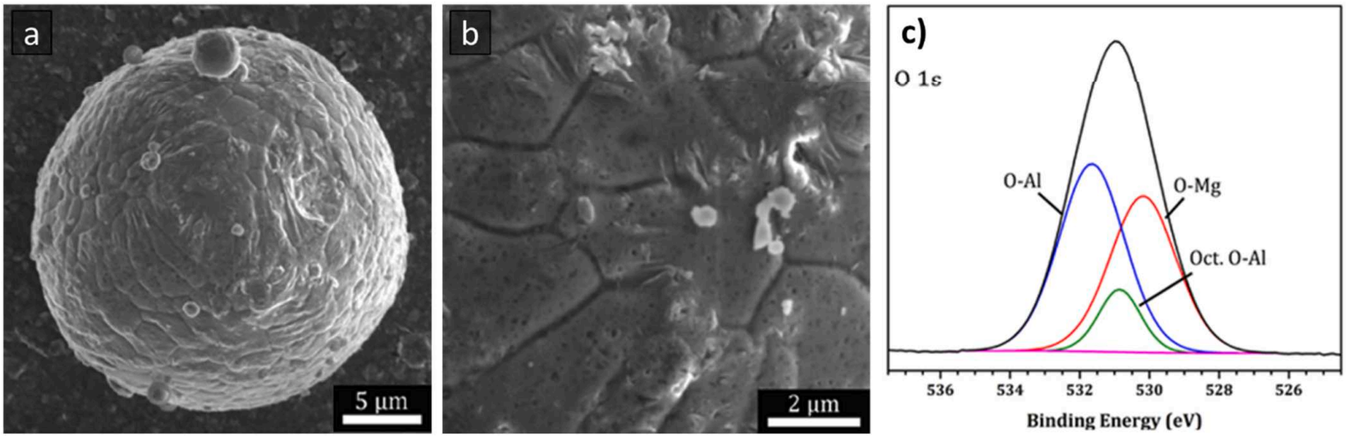

Fig. 1. (a) SEM image of gas atomized Al 6061 alloy powder particle. (b) microscale morphologies on the powder surface such as grooves and satellite particles and nanoscale pores. (c) O 1s XPS spectra showing surface oxidation of the Al 6061 alloy, averaged over areas larger than features in image (b). Reprinted from Applied Surface Science, 534, A.
T. Ernst et al., "Surface states of gas-atomized Al 6061 powders – Effects of heat treatment", 147643, Copyright 2020, with permission from Elsevier (Ernst et al., 2020).

improvements, and the wealth of information available from other spectroscopic techniques (Auger electron spectroscopy (AES) (described section 3.1.1), X-ray photoelectron spectroscopy (XPS) (described section 3.1.2)), there is still a disconnect in spatial localization between chemical information and ultra-high-resolution (UHR) SE images (Xing, 2016).

Previously, SEHI has been used to characterize the surface chemistry of polypropylene fibers in response to oxidation and tensile stress showing changes to fiber surface oxidation and molecular weight (Farr et al., 2021). Surface chemistry was related spatially to features such as cracks and shedding particles (formed on the surface of fibers).

Application of SEHI to fiber geometries indicate the technique can be translated to provide spatially localized powder surface chemical information. Nevertheless, the challenge remains of providing a reproducible technique for preparing powders for SEHI which are air and moisture sensitive, beam sensitive and insulating. LIB cathode and AM powder materials require preparation for SEHI in an inert gas environment such as a glovebox with the option of subsequent transfer to the SEM under vacuum or inert gas. Powder preparation techniques in literature for characterization by SEM as well as X-ray computed tomography (CT), AES and XPS are reviewed as candidates for SEHI preparation of powders in Section 4.3. Alternative preparation methods are found to be needed, and are trialed on commercial LIB cathode (lithiated nickel-rich layered oxide) and additive manufacturing powder feedstock (carbon fiber – polyamide-12 (CF – PA-12), CarbonMide®). The success of the trial is evaluated in terms adhesion, charging, particle-background segmentation and the ability to provide surface chemical analysis by SEHI. As SEHI is not yet widespread, practical aspects such as the selection of suitable imaging parameters in the LV-SEM and the conversion of the SEHI data volume into SE spectra are covered in Sections 5.3 and 5.4.

2. Powder characterization by LV-SEM

When a primary electron (PE) lands at a surface of a solid with a landing energy, E_L, it can free some electrons to produce delocalized SEs within the solid. Following this, inelastic and elastic interactions occur on the path of the SE through the solid causing further losses of energy. These numerous energy-loss interactions are termed the ‘energy loss cascade’ and define the energy distribution of SEs within the solid (Wolff, 1954). The inelastic interactions can also result in the emission of characteristic X-rays that can be used for EDX analysis. A schematic emission electron energy spectrum is shown in Fig. 3. LV-SEM imaging is commonly defined by having an electron accelerating voltage (AV) of < 2 kV (Butler et al., 1995). In the context of EDX analysis, an electron AV of < 5 kV may be considered low voltage (Asahina et al., 2015; Boyes, 1998). Secondary electron (SE), energy dispersive X-ray (EDX) and backscatter electron (BSE) emissions produced in the LV-SEM are discussed in the Sections 2.1 to 2.3 of the article. AES is discussed in Section 3.1.

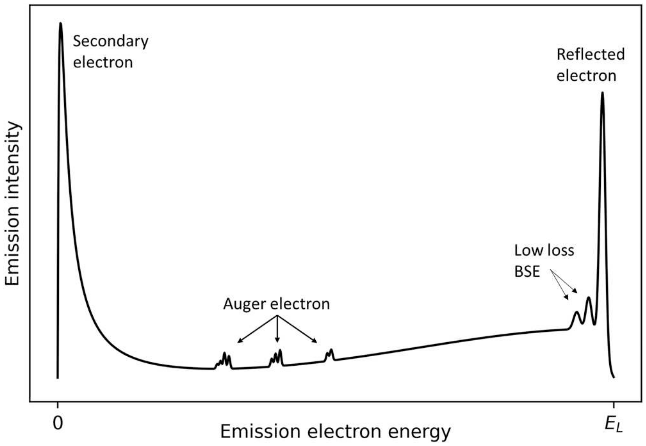

Fig. 3. schematic energy spectrum of electron emissions produced from a specimen irradiated by primary electrons (PEs) of landing energy E_L. Secondary electron (SE), Auger electron (AE) and backscatter electron (BSE) emissions are classed by their formation mechanism. Classification of a BSE into low-loss BSE and reflected electron are dependent on the energy loss mechanisms after formation. The emission electron has an energy characteristic of its formation and subsequent energy loss mechanisms. Thus, emission electron energy information can be used to characterize the specimen.

2.1. LV-SEM SE imaging

In brief, the SE emissions used for imaging are produced by a cascade of collisions initiated by the PE interaction. Collisions between delocalized electrons and bound electrons are inelastic scattering events. Each inelastic scattering event has an associated energy loss. By convention, SEs are defined by having a kinetic energy < 50 eV.

Working with AVs < 2 kV and low beam currents, enables the imaging of insulating and beam sensitive materials (Bell and Erdman, 2013; Liberman et al., 2020). Firstly, specimen damage and modification are related to the dose and E_L of PEs (Pawley, 2007). By decreasing

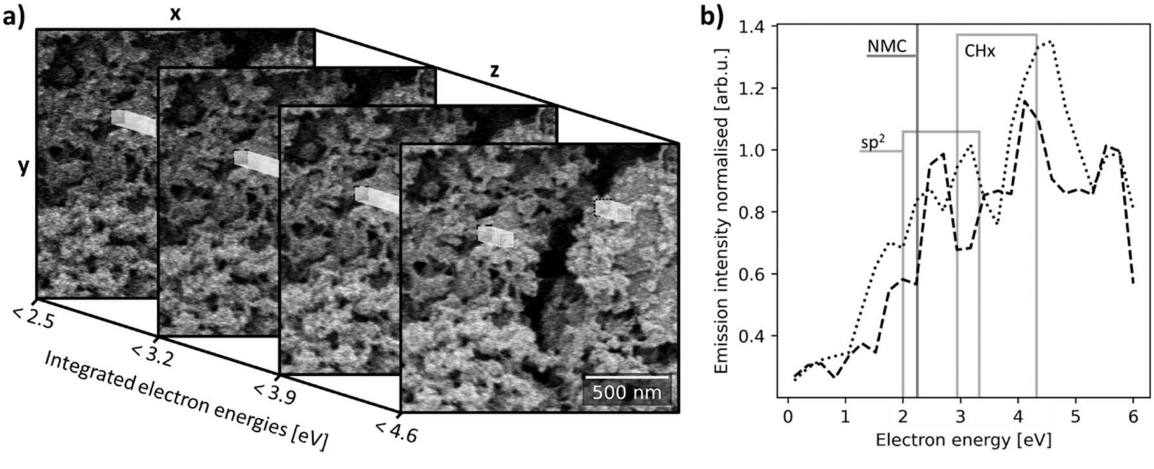

Fig. 2. (a) Image slices from a secondary electron hyperspectral imaging (SEHI) data volume of lithium-ion battery (LIB) cathode material. Images are formed of secondary electrons (SEs) up to a determined cut-off energy. The SEHI data volume has spatial (*x*, *y*) and energy (*z*) dimensions. (b) SE spectra are derived from square regions with 100 nm side length corresponding to the outlined regions in the SEHI data volume in (a). Since SE emissions have chemical contrast, the low energy SE spectra can provide spatially localized chemical information and qualitative comparison of surface chemistry at the nanoscale.

the energy of PEs, charging and heating of the specimen are diminished (Butler et al., 1995; Stehling, 2020), and in the LV-SEM regime the knock-on displacement damage mechanism is eliminated (Chen et al. give a threshold for knock-on displacement at an AV of 100 kV) (Chen et al., 2020; Egerton et al., 2004). However, radiolysis, the breaking of chemical bonds by electron-electron and electron-phonon inelastic scattering events, is exacerbated since the probability of inelastic scattering events increases (Egerton et al., 2004; Joy and Joy, 1996) – as evidenced by the maximum yield of secondary electron (SE) emissions occurring in the LV-SEM regime (Walker et al., 2008). This can have both positive and negative effects. As an example, cumulative damage by the image electron dose at 1 kV AV and 13 pA beam current was observed in pelletized perovskite solar cell material, methylammonium lead iodide ($MAPbI_3$) with 5 mol% excess methylammonium iodide (MAI). The damage is visible as grain boundary cracking and segregation of PbI_2 as images are sequentially taken in the same area (Figs. 4a-4c), increasing electron dose by $\sim 1.25 \times 10^{16}$ C/cm^2 in each image. In this particular case, the electron beam sensitivity is a good predictor of device stability. Beam damage to organic material was tracked during the measurement of polymer molecular order by SEHI (Masters et al., 2019). Using 200 ns and 50 ns dwell times, increased scan line integrations increased the electron dose. The result was that increased line integrations only modified polymer molecular order when the 200 ns dwell time was used. Using short dwell times to minimize damage is important, but equally important is the E_L. For instance, low E_L (0.5 keV) has been used to retrieve the pristine state of graphene surfaces by "desorption" of species produced by electron beam induced deposition (EBID) (Mikmeková et al., 2020). Secondly, the E_L can be used to control specimen charging to some extent. In theory for flat surfaces, the total emission current (of SEs and BSEs) can be balanced with the incident PE current to result in net neutral charging of the specimen (Joy and Joy, 1996; Wuhrer and Moran, 2016). However, local and temporal to the PE probe, the material can be in excited electronic states. Adjusting scanning parameters, such as scan interlace and dwell time, to distribute the electron dose of image acquisition in space and time can reduce the creation of local excited electronic states by allowing time for relaxation between doses (Stehling, 2020; Li et al., 2018).

Measurement of SE spectra, by SEHI or an in-chamber spectrometer, can provide information about the surface charging of specimens, by suppression of low energy emissions (positively charging specimen) or shifting emission peaks to higher energy (negatively charging specimen) (Stehling, 2020; Jbara et al., 2001). SE emission peak shift < 20 eV has also been modeled for 0.5 keV E_L electrons (Li et al., 2020). In reality, a powder surface presents a distribution of angled surfaces to the beam and thus the condition for charge neutrality might be very challenging to meet and depends on the powder diameter and embedding of the powder. Therefore, it is prudent to assume some charging will be present

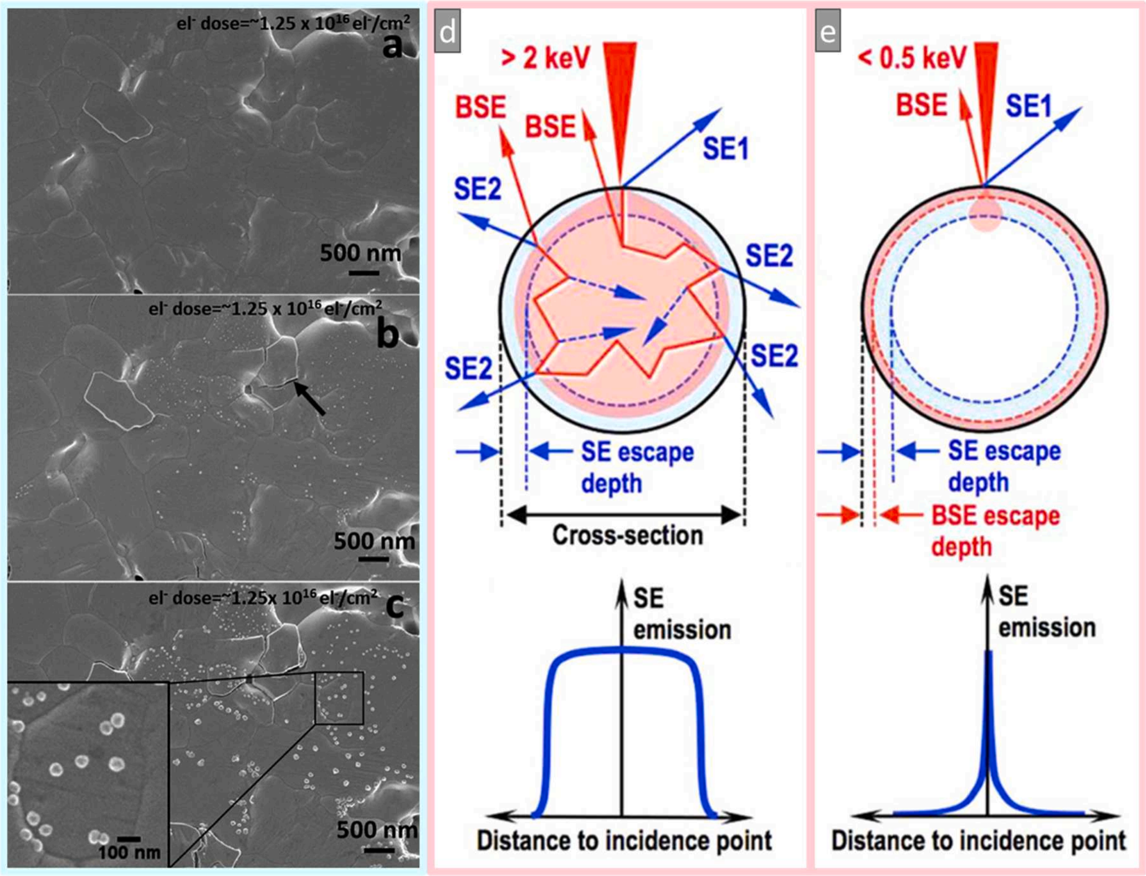

Fig. 4. (a-c) LV-SEM images from Kumar et al., "Stoichiometry-dependent local instability in MAPbI3 perovskite materials and devices" (Kumar et al., 2018), adapted by cropping under CC BY 3.0 license (https://creativecommons.org/licenses/by/3.0/legalcode), of 5 mol% MAI excess in $MAPbI_3$ pellet showing effects of cumulative electron dose (el-) from a-c such as cracking (black arrow in (b)) and growth of bright phases of PbI_2 (b-c). The electron dose per image is 1.25×10^{16} C/cm^2. By imaging in the same region, the dose cumulates a) 1.25×10^{16} C/cm^2, b) 2.50×10^{16} C/cm^2, c) 3.75×10^{16} C/cm^2. (d and e) schematics adapted by cropping from Zarraoa et al., "Imaging low-dimensional nanostructures by very low voltage scanning electron microscopy: ultra-shallow topography and depth-tunable material contrast", (Zarraoa et al., 2019) under CC BY 4.0 license (https://creativecommons.org/licenses/by/4.0/legalcode) showing the interaction volume and information depths of secondary electrons (SEs) and backscattered electrons (BSEs) from a nanoscale feature scanned by an electron beam with primary electron (PE) landing energy (E_L): d) 2 keV; c) 0.5 keV. Spatial localization of emitted electrons is improved by decreasing E_L. On reducing the accelerating voltage (AV) the information depth of the SE signal is unchanged, while the BSE information depth is a proportion of the PE interaction depth.

and to ensure that powders are well adhered to/ embedded in a substrate with good electrical grounding. Minimization of charging is essential for SEHI and also standard ultra-high resolution (UHR) SE imaging.

Much of the development in LV-SEM has come from the challenge to conduct UHR assays of beam sensitive semiconductor devices for quality control in the field of critical dimension (CD-) SEM (Lorusso et al., 2017). The principle of UHR imaging lies in the reduction of the interaction volume of PEs to the size of features being resolved (Stehling et al., 2018; Asahina et al., 2012; Seiler, 1983), as well as exclusion from detection of the SE emissions delocalized in time and space from the PE interaction (SE2 in Fig. 4d).

Reduction of the electron probe size at low AV is achieved by monochromation, which reduces the energy spread of electrons in the beam before focussing. For example the FEI UniColore (UC) monochromator produces a beam with < 0.2 eV energy spread (Young et al., 2008; Michael, 2011). Maintaining a small probe at low AV is also achieved by using a short working distance (WD) and employing an immersion lens (Young et al., 2008). These technologies allow LV-SEM imaging with sub-nanometer resolution (Michael, 2011; Vladár et al., 2009).

Fig. 4d shows how the intersection of the interaction volume by topography such as the particle edge will produce SE signal delocalized in time and space from the primary beam interaction (named SE2). Fig. 4e shows how a reduction of the E_L from 2 keV to 0.5 keV (produced by a 2 kV AV and 1.5 kV beam deceleration (BD) voltage) when interrogating nanoscale features does not reduce SE information depth but does improve lateral resolution by the reduction of SE2 emission.

LV-SEM SE signal extraction and detection using the through-lens detector (TLD) (sometimes called the in-lens detector) enables separation of the localized SE1 emissions for high resolution imaging (Vladár et al., 2009; Griffin, 2011). *Masters* et al. further improved the lateral resolution of SE images of polymer-fullerene photovoltaic blends to twice that achieved by a helium ion microscope (HeIM) by energy filtered detection of SE emissions in the LV-SEM using the TLD and WD of 3 mm (Masters et al., 2015). With the capability of UHR analysis of beam sensitive and insulating materials, LV-SEM has been used extensively to characterize powder and particulate morphologies in food (Burgain et al., 2017; Murrieta-Pazos et al., 2011), pharmaceuticals (Tsosie et al., 2017; Billi et al., 2009), health (Billi et al., 2009), environment (Willis et al., 2002) and energy storage (Kim and Park, 2021) sectors.

2.2. LV-EDX analysis

Production of fluorescent X-rays begins with the ionization of an atom, producing a hole in the atomic energy levels (Garrat-Reed and Bell, 2003). An electron occupying a higher atomic energy level subsequently transitions to fill the hole in the lower atomic energy level. The energy loss associated with the transition between energy levels is emitted as an X-ray. Thus emitted X-rays are characteristic of the occupied atomic energy levels.

For EDX analysis, the production of characteristic X-rays is the priority. For imaging the surface morphology of powders, beam voltage and spot size are optimized for highly localized SE emission. LV-SEM and EDX analysis were once considered incompatible: “Reducing beam energy and/or probe current […] is likely to conflict with the needs for EDX analysis” (Willis et al., 2002). For example, reducing beam voltage from 20 kV to 2 kV produces 35x less X-ray intensity from the Fe L-series (a typical beam for SE imaging is ~50 pA and 1 kV AV) (Burgess et al., 2017). The latest silicon drift detectors (SDDs) enable EDX analysis in the LV-SEM regime (LV-EDX analysis), primarily by being of the windowless design and having a large solid angle of detection (Burgess et al., 2017; Niculae et al., 2012). For example, to increase the solid angle of detection, the PNDetector Rococo2 X-ray detector is arrayed in four segments around the electron beam below the SEM pole piece (Niculae et al., 2012). At an optimum WD of 2.7 mm, the solid angle of detection is 2.4 sr. Conventional EDX detectors may have a solid angle of detection of 0.01 sr (Schoning et al., 2017). The effect of increasing the solid angle of detection was demonstrated by Hodoroaba et al. in the classification of SiO_2 nanoparticle chemistries (Hodoroaba et al., 2016). Nanoparticles were classified using a 5 kV AV and 216 pA beam current with a 1 sr solid angle annular SDD X-ray detector while 10 kV AV and 115 pA beam current was required when using a 0.006–0.007 sr conventional SDD X-ray detector. Windowless detector designs were sought to detect the X-ray spectrum below 1 keV, since the window placed over X-ray detectors could absorb a portion of the low energy X-rays (Llovet et al., 2021). Windowless detectors aid LV-EDX analysis since emission X-rays do not exceed the PE E_L (Yamamoto et al., 2016). Reduction of electronic noise in detector circuitry has also enabled higher maximum count rates in the latest X-ray detectors (Pinard et al., 2018).

With these developments in X-ray detectors, high spatial resolution elemental mapping detectors offered by detectors such as the Oxford Instruments Ultim® Extreme and PNDetector Rococo2 can be combined with field emission LV-SEM instruments developed for UHR BSE and SE imaging (Schoning et al., 2017; Oxford Instruments, 2019). Example applications include the phase analysis of metal oxide segregation in ferrocerium nanoparticles (Fig. 5a) and “yolk” Au nanoparticles in a TiO2 “shell” framework (Fig. 5b).

Despite advances in the LV-EDX detectors, physical limitations to X-ray emission in LV-SEM still exist. Versus SE yield, fluorescent X-ray yield is approximately one hundred thousand times less per PE (Joy et al., 2004; Prasad and Joy, 2003), and the beam current and acquisition time required to make the LV-SEM EDX elemental maps like those in Fig. 5 are prohibitive to the analysis of many beam sensitive or insulating powder materials (Rasch et al., 2014). For example, the map of Au nanoparticles in a TiO_2 framework was acquired over 10 min with 220 pA beam current and 4 kV AV (Figs. 5b and 5c) while a SEHI data volume can be acquired using roughly a quarter of the beam current (see instrument parameters for SEHI Section 5.3, Table 3). Despite the escape depth of fluorescent X-ray emissions being up to a few micrometers (Small, 2002), examples of ultra-high spatial and depth resolution EDX maps such as that of Fig. 5a are achieved by reducing the interaction volume of the PEs to within 10 nm of the metal surface. Ti peak intensity in X-ray energy spectra produced using a 3 kV AV and 1 nA beam current was shown to be sensitive to a 2.4 nm TiN film deposited on a silicon wafer (Shemesh et al., 2011). Nagoshi et al. show that increasing AV from 1.5 kV to 10 kV causes a loss of B, O and Mn characteristic X-rays from features ~ 100 nm in width (Nagoshi et al., 2017) and in doing so the information depth of X-rays is limited first by the interaction volume of the PEs and then the escape depth of X-rays. Similarly, with a 15 nm carbon coating on a nickel substrate, Boyes shows that bulk or near surface chemical analysis can be selected by varying beam AV from 1.5 kV to 20 kV (Boyes, 1998). However, a disconnect in the information depth of EDX maps and SE images can exist. This is because the information depth of SEs with kinetic energy < 50 eV, considered to be the mean escape depth (MED) of the SEs (Seiler, 1983; Zou et al., 2016; Hussain et al., 2020), is significantly less than the interaction depth of the PEs in the material. The MED of SEs from Si and Au was calculated to be between 0.75 and 2.4 nm and 0.3–0.55 for a range of E_L between 0.1 and 5 keV (Zou et al., 2016).

2.3. LV-BSE imaging

Like the production of X-rays, the information depth of BSEs is determined by the depth of the PE interaction and not the BSE escape depth (Figs. 4d and 4e). The information depth of BSEs has been modeled to be 0.2–0.5 times the interaction depth of PEs and measured to be 0.27 times the interaction depth of PEs in a steel specimen (PiŇos, MikmekovÁ and Frank, 2017). Exploiting this variable information depth, BSEs produced by PEs with 0.5–3 keV landing energy (E_L) were used to characterize through the thickness of a poly(3-hexylthiophene) (P3HT) organic photovoltaic (OPV) material over depths of

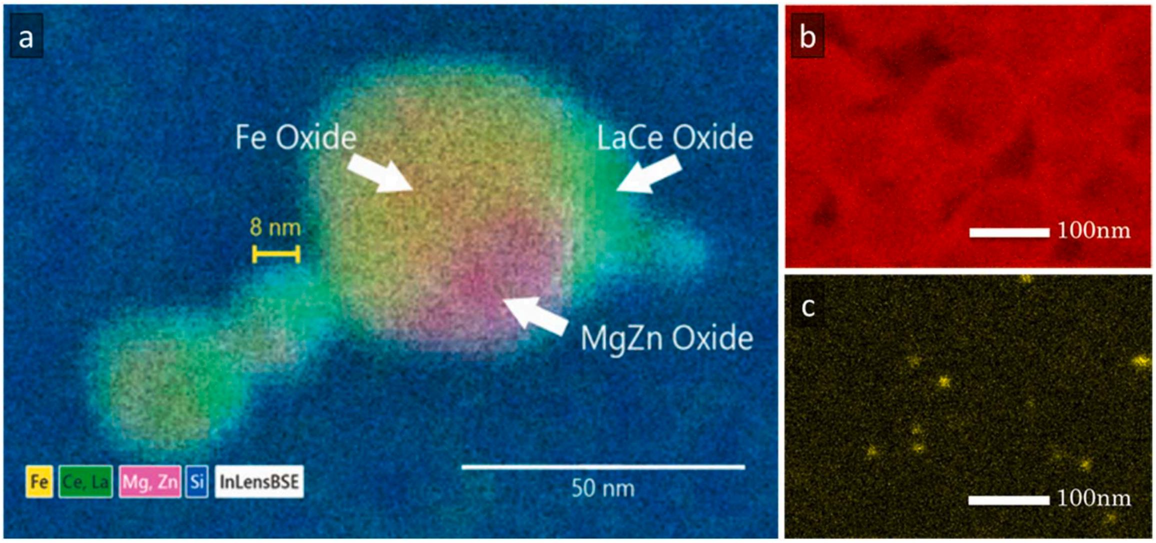

Fig. 5. LV-SEM EDX maps of metal nanoparticles. a) cerium nanoparticles collected with 2 kV AV over 5 min overlayed on a BSE image. (b and c) yolk-shell catalytic material of Au nanoparticles in a cross sectioned TiO_2 matrix collected with 4 kV AV and 220 pA beam over 10 min where b is formed of O K-line X-ray emissions and c is formed of Au M-line emissions.
(a) Reproduced from (Burgess et al., 2017) Burgess et al., "Ultra-Low kV EDS – A New Approach to Improved Spatial Resolution, Surface Sensitivity, and Light Element Compositional Imaging and Analysis in the SEM", Microscopy Today, 25, 2, 20–25, with the permission of Cambridge University Press. (b) Reproduced from Asahina et al. "Direct observation and analysis of york-shell materials using low-voltage high-resolution scanning electron microscopy: Nanometal-particles encapsulated in metal-oxide, carbon, and polymer" (Asahina et al., 2014) under CC BY 3.0 license (https://creativecommons.org/licenses/by/3.0/legalcode).

~10–150 nm.

A combination of detectors, beam deceleration (BD) fields and WD variation can be used to produce and select BSEs with topographic or materials contrast. Zarraoa et al. produced images of silicon nanowires optimized for atomic weight contrast, depth-tuneable material contrast or resolving surface nanostructures (Zarraoa et al., 2019). UHR images of topography were formed from high-angle BSEs using PEs with $E_L = 0.5$ keV. The E_L was controlled by a 2 kV beam AV and BD voltage of 1.5 kV applied to the specimen holder. It should be noted that while BSE imaging is demonstrated on complex geometries such as the silicon nanowire, imaging conditions place constraints on the analysis of powder materials. In the BD fields applied to the specimen, negatively charged particles are attracted towards the column where they may produce stray fields additional to the electron optics. Therefore, a reliable powder preparation for SEHI will also be valuable for BSE imaging.

2.4. Summary of powder characterization by SEM

In the LV-SEM, SE, X-ray and BSE signals are used for topographic and chemical contrast imaging (SE imaging), elemental composition mapping (EDX analysis) and atomic weight contrast and topographic imaging (BSE imaging). This information is even available for materials with complex geometries, like powders. Nevertheless, present chemical characterization of powder particles has been shown to be limited to elemental mapping of conductive materials resistant to beam damage. Chemical information provided by LV-EDX analysis and LV-BSE imaging is also limited to elemental mapping and atomic weight contrast. Other spectroscopic techniques such as AES and XPS (discussed in Section 3) must be used to provide chemical bonding information.

Information provided by LV-SEM is summarized in Table 1. The provision of chemical bonding contrast in SE emissions, high spatial resolution and high yield of SEs in the LV-SEM goes some way to explain the unique capabilities of SEHI for surface chemical analysis. The high SE yield enables low beam current to be used for analysis of beam sensitive and insulating materials. Although the depth resolution of SEs is currently limited by the material characteristic MED, spatial resolution of SE imaging may surpass that of LV-EDX to resolve powder surface nanostructures. SEHI characterization of powder materials is reviewed in Section 4 and practically applied in Section 5.

3. Powder surface chemistry characterization by spectroscopies exploiting electrons

AES and XPS are useful techniques for chemical characterization of powder surfaces (Galvão et al., 2018). As we propose SEHI as an alternative technique to conduct spatially localized surface chemical characterization in LV-SEM conditions, in the following sections we compare SEHI to AES and XPS.

Auger electrons (AEs) and photoelectrons are produced when a specimen is irradiated by X-rays (Woodruff, 2016). AEs are also

Table 1
Comparison of SE, EDX and BSE signals in LV-SEM from example studies.

Emission type	Energy	Information		Beam current	Yield from C at $E_L = 1$ keV	Resolution	
		Topographic	Chemical/ elemental			Spatial	Depth
SE	< 50 eV (by convention (Seiler, 1983))	✔	Chemical	50 pA (this work)	0.47–0.62 (Walker et al., 2008)	0.8 nm (Masters et al., 2015)	0.3–3.3 nm (MED) (Zou et al., 2016)
X-ray	$< E_L$	✖	Elemental	220 pA (Asahina et al., 2014)	(generally ~ 10^{-4} (Prasad and Joy, 2003))	< 10 nm (Burgess et al., 2017)	Tuneable with E_L
BSE	$< E_L$	✔	Elemental	100 pA (Zarraoa et al., 2019)	0.10 (el Gomati et al., 2008)	~ 3 nm[a] (Zarraoa et al., 2019)	Tuneable with E_L

[a] measured using the edge resolution method in Reimer (Reimer, 1998)

produced by electron irradiation. AEs result from a series of two ionizations events while photoelectrons result from a single ionization event (Stevie and Donley, 2020). AEs and photoelectrons contain information about occupied energy levels in the specimen. AEs and photoelectrons also provide information about local chemical bonding since the transition and emission electrons can originate from energy levels affected by the electronic structure of neighboring atoms (Tougaard, 1998). AEs and photoelectrons have short inelastic mean free paths (IMFP), which is the average distance an electron with a given energy travels between successive inelastic collisions (International Organization for Standardization, 2013). Since only electrons that travel from their emission point to the surface without inelastic collision will contribute to the characteristic peaks, the short IMFP translates into high surface sensitivity. The inelastic scattering events that occur during transport to the specimen surface modify the peak shape of the electron energy spectra (Tougaard, 1998).

3.1. AES

The emission process begins with the first ionization by incident radiation, which removes an electron from a core energy level of an atom. An electron transitions from a higher energy level into the hole in the core energy level. The energy lost in this transition is characteristic of the energy levels that the electron moves between. The characteristic energy is then transferred to another electron which causes a second ionization event. The AEs or photoelectrons produced by the second ionization event are detected with energy and count rate information which contains chemical information about the specimen (Watts and Wolstenholme, 2003). In AES, energy levels are given X-ray notation. For example, the C *KVV* peak centered at 264 eV, used to show carbon allotropes have similar sp^2 bonding, relates to a hole in the *K* (1s) level being filled by a valence band electron causing a valence band electron emission (Lu et al., 2021). However, Lu et al. conclude that chemical shifts observable in the AES peaks as result of plasmon losses during the migration of the AE to the surface are too subtle to be used as a measure of long-range order to differentiate sp^2 bonded carbon allotropes (Lu et al., 2021). Nevertheless, AES measurements on graphite particles in electrochemically lithiated graphite anodes, exhibit clear line shape changes in the C *KVV* peak from band-like (graphitic) character to atomic-like (carbidic) character due to the Li intercalation (Ishida et al., 2014).

If the incident electron beam can be scanned as in the SEM, scanning Auger Microscopy (SAM) can be conducted for chemical mapping. For instance, SAM was used to map the lithiation of a graphite powder LIB anode at 100%, 50% and 20% states of charge (Ishida et al., 2014). However, the SAM did not provide sufficient spatial resolution to reveal the conductive additives. SAM may provide high spatial resolution information if combined with morphological information obtained from the SEM images. For example, the Sulfur distribution in a bulk organic heterojunction solar cell material was found to be distributed non-uniformly. It appeared to correlate with the surface morphology on a 20 nm scale shown in the corresponding SEM image (Heon Kim et al., 2014). While the lateral resolution in dedicated SAM instruments tends to be lower than that achievable in dedicated high resolution SEMs, SAM does offer high surface sensitivity.

Chang reports that AEs are emitted from the first five monolayers of atoms and that to AES chemical analyses of the surface in the desired condition requires dedicated instruments with ultrahigh vacuum (UHV) conditions and in-situ cleaning (Chang, 1971). A study of SiO_2 and TiO_2 nanoparticles was able to meet bulk chemical, morphological and size characterization requirements in a SEM instrument, but required a scanning AE microscope for particle surface chemical characterization (Rades et al., 2014). This is in part because AEs have a lower yield compared to SEs, reported to be $\sim 10^{-5}$ times less than the beam electrons in experiments (Finello and Marcus, 1979), whereas the SE yield in LV-SEM is near 1 for many materials (Wuhrer and Moran, 2016). Beam parameters selected for AES are typically around 5 kV AV and 10 nA is given as a low beam current for analysis of insulators by Hofmann (Hofmann, 1992). Increasing electron dose results in increasing surface contamination (Vladár and Postek, 2005). The surface sensitivity of AES and relatively high electron doses (compared to LV-SEM) required for SAM risks that measurements are influenced by surface contamination deposited during the measurement (Takeichi et al., 1996). Most SEMs do not operate under UHV conditions. Thus, surface chemical characterization in vacuum conditions similar to SEM would require much lower electron doses (shorter acquisition times and low beam currents). For a given detector collection efficiency, this is only feasible for sufficiently high electron yield. SE spectra collected in LV-SEMs could potentially provide an alternative to AES, provided sufficient chemical information is contained in SE spectra. Section 4.1.1 reviews chemical information in the SE spectrum. A practical implementation of SE spectra collection within dedicated UHR SEM columns to enable SEHI and thus high-resolution chemical mapping is introduced in Section 5.

3.2. XPS

Modern instruments often combine AES/SAM with XPS (Isaacs et al., 2021). The spatial resolution of XPS is limited to the X-ray beam diameter. For laboratory soft X-ray probe (< 6 keV) instruments this is on the order of 10 μm (Scheithauer, 2008). The spatial resolution of XPS has been reduced below the beam diameter by locally charging the specimen with an electron beam. Photoelectron spectra in the charged region have a differential shift in energy compared to spectra produced within the rest of the 100 μm X-ray probe (Scheithauer, 2020). XPS was coupled with LV-SEM SE and BSE images to infer the spatial distribution of surface chemistry of natural fibers beyond the resolution of XPS analysis (Rasch et al., 2014).

While low spatial resolution might be a limitation to XPS surface analysis, the extraction of qualitative and quantitative information about surface chemical bonding is well developed. Intense peaks formed by photoelectrons which undergo one or two inelastic scattering events prior to emission are easily separated from the background emissions which undergo a cascade of inelastic scattering events (Engelhard et al., 2020). This background can be subtracted in a linear region, and a non-linear Shirley background around the peak (Engelhard et al., 2020). XPS gives highly detailed spectra with details from all occupied energy levels in the specimen. XPS may also be carried out on insulating and beam sensitive materials, inaccessible to AES (Stevie and Donley, 2020). Electron and ion flood guns are used to charge compensate the sample which would otherwise become positively charged through emission of electrons (Wood and Teeter, 2018). However, for powder materials additional measures are often required. Particular attention has to be paid to powder sample preparation for XPS (Baer et al., 2010). While powder mounting strategies have been evolved over decades, soft, brittle and air sensitive powders such as encountered in LIB cathodes and polymer AM pose new challenges, see Section 5.1.1.

3.3. Summary of powder surface chemistry characterization by spectroscopies exploiting electrons

AES and XPS provide detailed information about the occupied energy levels of the specimen including chemical shift which contains information about chemical bonding. The mechanisms of AE and photoelectron formation and subsequent energy losses are well understood and thus spectrum peaks are easily separated from the background for quantitative analysis. While XPS provides chemical bonding information averaged over ~10 μm, AES can provide spatially localized chemical information at the nanoscale. However, the low yield of AEs necessitates the use of high beam currents which is prohibitive of the analysis of insulating and beam sensitive material. UHR LV-SEM instruments are not typically used in UHV mode either. Since it is desirable to carry out surface chemical characterization using the LV-SEM to achieve better spatial resolution, the higher yield SE signal should be used, provided that chemical contrasts in SE emissions can be extracted and SE spectra can be produced. The following sections review the feasibility of using the LV-SEM for surface chemical characterization of powder materials and finally offer practical application of SEHI to characterize powder materials.

4. Feasibility of using the LV-SEM for surface chemical characterization of powder materials

4.1. SE spectroscopy

4.1.1. Chemical information in SE spectra

To understand the general shape of the SE emission spectrum, it is helpful to describe the emission of SEs into the vacuum as occurring in three steps. Firstly, the freeing of bound electrons by PEs produces delocalized SEs within the solid. Secondly, inelastic and elastic interactions that occur on the path of the SE through the solid cause further losses of energy. These numerous energy-loss interactions are termed the 'energy loss cascade' and define the energy distribution of SEs within the solid (Wolff, 1954). Finally, the onset of the SE emission spectrum is related to the energy required for SEs to overcome the surface energy barrier and has been modeled by the surface threshold function - empirically determined by Seah (1969).

Models of the SE spectrum in the range < 50 eV have been used to calculate the maximum peak position in the SE emission spectra, which generally occurs in the low energy range < 10 eV. SE emission peak position in this range has been found to be constant with varied PE energy (Schafer et al., 1981). Chung and Everhart calculated the maximum SE emission peak position for Au and Al to be within the 1.3–2.5 eV range present in experimental SE spectra, at approximately one third of the work function (φ) of the material (Chung and Everhart, 1974).

However, these models of SE spectra do not include the 'fine' spectral structures observed in experimental low energy SE emission spectra (with energy resolution <0.5 eV) which are superimposed on the background SE emission energy distribution (Willis and Christensen, 1978; Willis and Fitton, 1972). These SE spectroscopy experiments related the fine structure in SE spectra to the band structure of the material by comparing fine structure peaks to the surface and bulk density of states (DOS) distributions. To closely compare the fine spectral features to the DOS distribution, various approaches to subtract the background signal from SE spectra have been attempted. *Willis* subtracted the *Seah* model of the background but abandoned this approach when it produced negative intensity in some spectra, instead opting to subtract an arbitrary linear background to produce 'enhanced DOS profiles'. These experimental 'enhanced DOS profiles' consistently contain an SE emission minimum over the energy range of the band gap. Lately a 'SE spectral DOS signal' has been extracted by subtracting the normalized SE spectrum taken with a 1 kV AV from the normalized SE spectrum taken with a 0.5 kV AV (in which the fine spectral signal is more pronounced) and then differentiating this difference spectrum with respect to SE energy (Han et al., 2020). All SE spectral DOS signals produced by this method showed $< 7\%$ normalized root mean square deviation (NRMSD) versus the bulk valence band DOS distribution. Additionally, energy loss features - two troughs that deviate from the DOS distribution signal - in the SE spectral DOS from aluminum were attributed to SE interactions with surface and bulk plasmons (Han et al., 2020).

Recently, a Monte Carlo modeling approach has included 'SE spectral DOS signal' fine spectral features. The MAterial Simulation Toolkit for Secondary Electron Yield (MAST-SEY) models low energy electron inelastic scattering energy losses from first-principles density functional theory (DFT) calculations (Polak and Morgan, 2021). In comparison of these models to experimental SE spectra, Polak and Morgan note that a real sample with surface roughness and inhomogeneities can obscure the DOS features. Thus, high spatial localization of SE emission and detection is needed to compare regions of differing chemistry and topography.

4.1.2. SE spectrometers

The instruments for AES and XPS spectroscopy are optimized for high resolution electron energy spectra. For XPS, the energy resolution of high resolution scans around specific peak energiesis limited by the X-ray linewidth and can be 0.26 eV for monochromated Al Kα radiation (Stevie and Donley, 2020). However, the beams in these instruments are not optimized for spectral imaging and tend to lack the high spatial resolution available in modern LV-SEMs. An approach for combined spatial and energy resolution is to incorporate an SE energy analyser into the SEM chamber or column. Dedicated SE energy analysers have the benefit of collecting the SE energy spectrum in parallel; dispersing SEs by energy to different detector channels for simultaneous detection (Khursheed, 2020). The multi-channel SE off-axis analyser built by Kienle and Plies uses 1280 channels to detect SEs over 0–20 eV simultaneously, collecting a complete spectrum in 0.5 s (Kienle and Plies, 2004). Similarly, the in-chamber toroidal energy analyser attachment can either generate a spectrum over a scan area or spectra for each pixel in an image (Han et al., 2020; Srinivasan et al., 2021). Until now the image mode has had limited use due to the EBID caused by serial image acquisition in the same area (Srinivasan et al., 2021). Approaches to disperse electron dose in space and time discussed in Section 2.1 may overcome this to deliver high resolution SE energy spectra with nanoscale spatial resolution in future.

4.2. Using TLD imaging systems in SEMs to extract SE spectra

The imaging performance of LV-SEMs has been improved in recent decades by introducing TLD or in- lens detection designs that allow UHR imaging as well as energy filtering capabilities. Of the multiple designs it was shown that the TLDs in XL30 column and Elstar SEMs columns can be utilized as a low pass filters in SE imaging (Masters et al., 2015). The relevant schematics for these designs are shown in Figs. 6a and 6b respectively. In these detectors, SE emissions from the specimen are guided back through the objective lens by using an extraction/suction tube. The extraction field (produced by the extractor/suction tube) skews SEs emitted from the sample surface in all directions towards the optical axis while deflector/push electrodes are used to deflect SEs towards the scintillation detector. In the simpler XL30 column design the deflector voltage is adjusted to determine the maximum energy of SEs that can be detected (Rodenburg et al., 2010). Higher imaging resolution is obtained with the Elstar column in which the extracted SE are reflected by a (variable) mirror electrode prior to being pushed towards the scintillation detector. The systematic variation of deflector/mirror voltage respectively allows for collection of an image series with variable high energy cut-off. Thus, these systems can be used as low-pass filter to produce S-curves which can be differentiated to obtain SE spectra.

However, simulated acceptance diagrams for the XL30 design reveal that SE spectra obtained in this way can be distorted, especially in the region of high energy SEs (Rodenburg et al., 2010). Experimental S-curves obtained using an Elstar column shown in Fig. 7a demonstrate the presence of distortions of the S-curve when a bias is applied to the specimen. The negative bias accelerates emitted electrons and thus shifts the S-curve to higher energy (Kazemian et al., 2007). In an ideal system, a -1 V bias is equivalent to 1 eV gain in kinetic energy. For comparison, Fig. 7b contains S-curves that would be expected from an ideal spectrometer in which the application of a sample bias would solely result in a shift of the S-curve by ΔV_R, the difference between biases V_{S1} and V_{S2}. While a shift is observed in Fig. 7a, it is also accompanied by changes to the shape of the S-curve.

More recently Khursheed reviewed in detail approaches to adapt the LV-SEM TLD detectors for SE spectroscopy and also concludes that

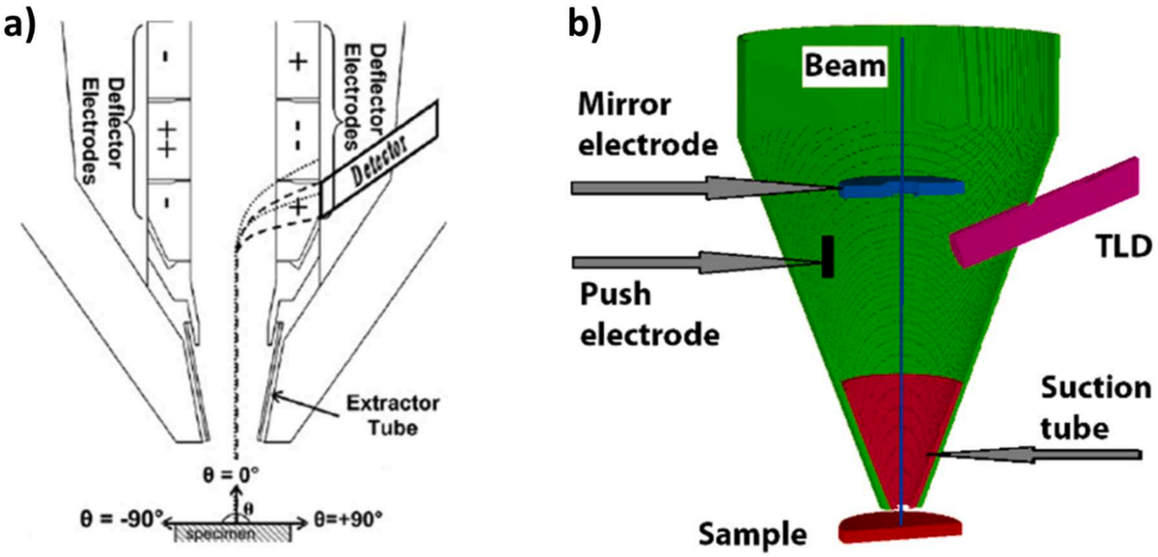

Fig. 6(. a) XL30 column energy filtering principle adapted from Rodenburg et al., "Energy filtered scanning electron microscopy: Applications to characterization of semiconductors" (Rodenburg et al., 2010) by rotating figure labels under CC BY 3.0 license (https://creativecommons.org/licenses/by/3.0/legalcode). (b) Elstar column energy filtering principle from Konvalina et al., "In-lens band-pass filter for secondary electrons in ultrahigh resolution SEM" (Konvalina et al., 2019) reproduced under CC BY 4.0 license (https://creativecommons.org/licenses/by/4.0/legalcode).

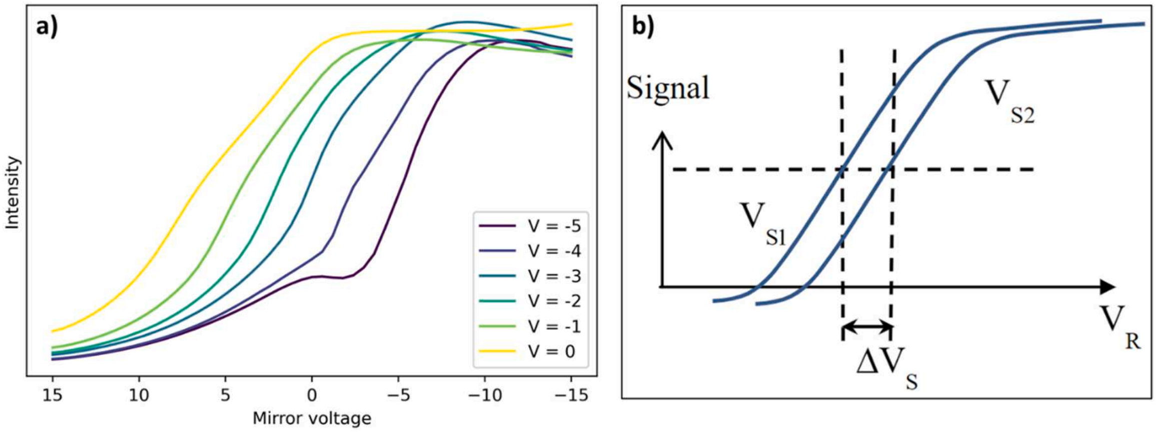

Fig. 7. (a) experimental S-curves at varied stage biases (V) from a Helios NanoLab G3 UC SEM with Elstar column, showing variation in S-curve shape with stage bias. (b) theoretical output S-curve from an ideal SE spectrometer (closed loop retarding field spectrometer) showing the offset in S-curves with identical shape between biases and from Khursheed A., "Energy Analyzer Attachments for the Scanning Electron Microscope", Microscopy and Microanalysis, 21, S4, 130–135, reproduced with permission from Cambridge University Press (Khursheed, 2015).

inherent limitations of these detectors result in detection of SEs of varied emission angles and energies which results in 'distorted and truncated' SE energy spectra (truncated at 6–7 eV) (Khursheed, 2020). However, distortion and truncation of SE spectra produced by in-lens energy filtering could arguably be of relatively little consequence in practical applications because the spectral region of interest is in the low energy range, where the DOS most effected by chemical shifts exist (Han et al., 2020). Secondly, the low energy SE emissions appear to be less effected by topography. The energy below which topographic information is minimal has been established experimentally for two systems. Kumar et al. produced S-curves from two TiO_2 film morphologies, showing similar emission intensity in the 0–4 eV region (Kumar et al., 2017). Stehling et al. supressed topographic contrast in images of ramie plant fiber by producing an image of chemical contrast made of 0–3.5 eV SE emissions (Stehling et al., 2018).

LV-SEM with energy filtered detection has gone beyond characterization of surface morphology to be able to conduct micro- to nanoscale chemical analyses of materials surfaces. This capability includes creating surface chemical maps (Masters et al., 2019; Farr et al., 2021, 2020). The technique has evolved from the use of LV-SEM instrumentation with energy filtered detection of SEs for imaging dopant contrast in semiconductors (Schönjahn et al., 2002; Hashimoto et al., 2020) to SEHI. SEHI is a method of using energy filtered SE detection to build an SE spectrum per pixel location in the image (Nohl, 2020; Stehling et al., 2018).

Through suppression of topographic SE contrast, also a major concern in SAM (Roberts et al., 1997), production of SE emission spectra in the low energy region paves the way to chemical mapping using SE images formed within a well specified energy window. Since the SE1 escape depth is predominantly within 5 nm of the material surface (Lin and Joy, 2005), surface chemical information is extracted at the same length scale as, and can be associated with, UHR SE images. The following section acts as a guide to the application of SEHI to powder materials and extraction of surface chemical information with high spatial resolution.

4.3. Powder preparation methods

As discussed in Section 2.1, issues such as charging and beam induced damage are encountered when imaging and analysing powder specimens with the SEM. SEHI adds new risks and constraints to powder analysis, particularly the motion of charged particles in the extraction field into the SEM column. Charged particle detachment and its results are summarized in Fig. 8. Generally, stage bias is not applied during SEHI (except for energy calibration purposes described in Section 5.2), since the lowest energy SEs have most chemical information and SE emission intensity is calibrated to SE emission energy at a given extraction field. Given a beam AV of 1 kV, specimen charging is further mitigated by using low beam currents (~ 50 pA), short beam dwell time (< 100 ns) and scan interlace patterns that distribute the electron dose in time and space (Stehling, 2020). Bright spots in the image are early warning signs of unsuccessful powder preparation causing particles to negatively charge in the beam (Postek and Vladár, 2015) (Fig. 8c), which may lead to particle detachment and attraction into the optics column (Fig. 8b). Contamination of the optics by charged particles will produce meaningless results due to the stray electric field around the particle (Fig. 8d). Nevertheless, the information to be gained from SEHI analysis of powder specimens makes development of a failsafe powder preparation method worthwhile.

Besides the risks posed by charged particles, SEHI adds challenges to specimen preparation due to the technique's surface sensitivity. SEHI has been used to measure the carbonaceous species produced by aging in air on a graphite surface (Abrams et al., 2019), as well as in-chamber contamination in FIB-SEMs (Farr et al., 2021). For air-sensitive material surfaces to be observed in pristine or application condition the preparation method must be 'dry' – involving no volatiles or suspensions – and be compatible with working in a glovebox. The surface sensitivity of SEHI prevents the use of solvents as suspending agents for powder dispersion (Asahina et al., 2015; Ogi et al., 2007; Demers et al., 2015; Crouzier et al., 2021) due to the surface sensitivity of the technique to surface functionalisation and oxidation (Farr et al., 2020; Abrams et al., 2019; Rodenburg et al., 2010).

With these constraints in mind Table 2 has been produced, which summarizes powder preparation techniques. The findings of the search for applicable powder preparation techniques reveals only two methods that might be applicable for both SEHI and the glovebox. While the

Table 2

Methods of powder preparation reported in literature and this work with a view to their compatibility to surface-sensitive SEHI analysis.

Method	Reported	Glovebox compatible?	SEHI compatible?
Dry dust 'puffer'	(Willis et al., 2002)	Requires gas flow inlets/ outlets	Not tested
Wet dust 'puffer'	(Willis et al., 2002)	✖	✖
Kapton tape	(Heenan et al., 2020)	✔	✖
Carbon tab	Common	✔	✖
Grooved-carbon stub	(Tsutsumi et al., 2014)	✔	✖
Colloidal solution	(Asahina et al., 2015), (Ogi et al., 2007; Demers et al., 2015; Crouzier et al., 2021)	✖	✖
FIB Pt deposition	(Walde et al., 2018)	✔	✖
Pressed indium foil	(Baer et al., 2010), (Ro and Linton, 1992), (Salvi et al., 1995)	✔	Not tested
Cold pressed pellet	This work	✔	✖
In Field's metal	This work	✔	✔

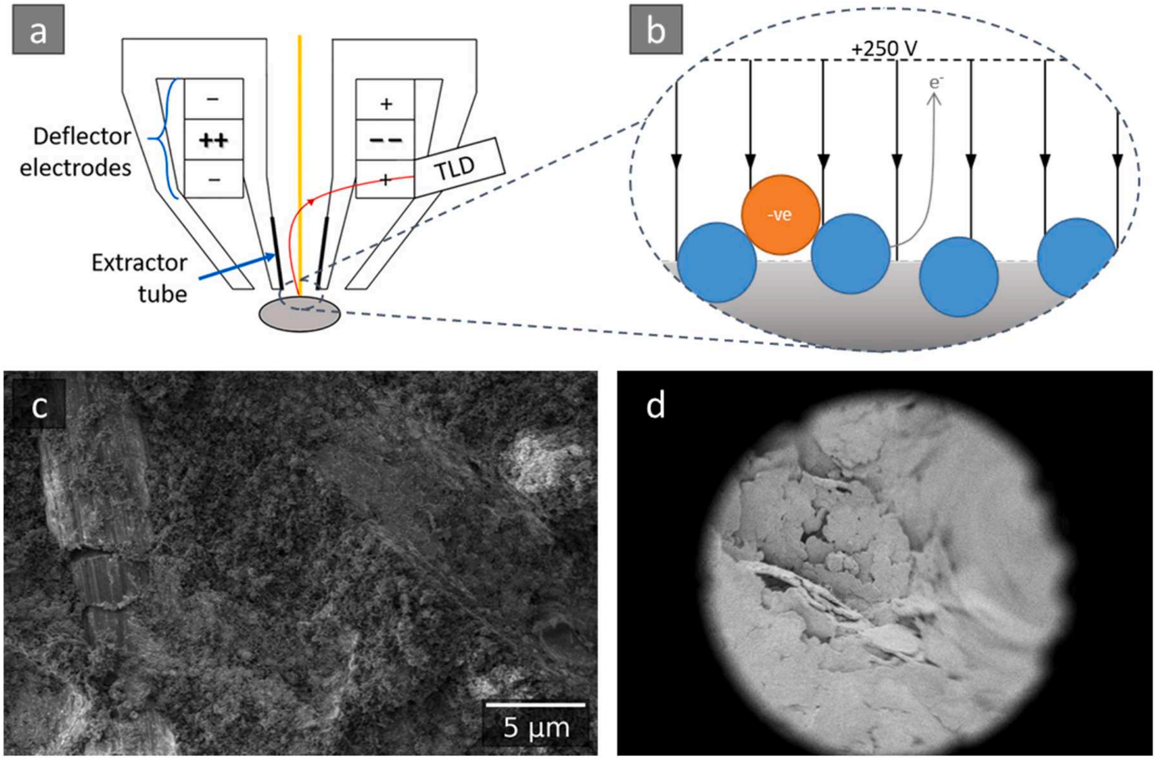

Fig. 8. SEHI and powder samples – complications arising from charged particle motion by the extraction field. (a) layout of through lens detector in the optic column reproduced from (Nohl, 2020). (b) A negatively charged particle will be attracted towards the optics column by the extraction field. (c) bright spots and distortions in an image are indicative of poor specimen grounding contact. (d) Operating with a charged particle in the optics column will give meaningless results due to image distortion – clearly visible in the right of the image through the pole piece formed by the TLD.

pressed indium foil preparation used for XPS studies offers good electrical contact, the high purity indium foil is chosen for its reproducible signal which must be subtracted from the spectra produced from powder specimens, since in XPS the photoelectron emissions are produced and detected with low spatial resolution. The indium foil preparation method is described in detail by Baer et al. as a means of preparing particles and fibers for AES (Baer et al., 2010). By using the Field's metal alloy for SEHI preparation, the cost per sample is drastically reduced vs using high purity indium. Walde et al. prepare particles for plasma-FIB milling by depositing Pt over the particle of interest with the FIB (Walde et al., 2018). The plasma-FIB milling then removes the deposited Pt and exposes a cross section of the particle. Other methods for powder preparation reported by Walde have issues: particle charging and movement when particles are dispersed on Cu tape; poor distinction of particles from carbon paint and outgassing from carbon paint.

Powder specimens for SEM can either be in the form of bulk powders such as pellets or dispersed in embedding media or on a substrate. Given the utility of SEM for quantitative analysis of particle size, the latter is preferred as it will produce high contrast between particles and the substrate. The substrate/embedding media should provide good contrast between particles and substrate since particle or edge like features can be identified by automatic particle measurement algorithms (Willis et al., 2002). Successful particle and fiber segmentation in a specimen prepared by the Field's metal embedding method presented in this article (Section 4.3). These powder preparation techniques involve a powder dispersal step to produce a monolayer of particles which will all be in contact with the substrate. Reproducible powder dispersion is also essential for quantitative particle size analysis. Preparations can skew results by selecting for large or small particles (Billi et al., 2009). For SEHI specimens, producing a monolayer of particles will also result in all particles having electrical contact with the substrate.

5. Practical implementation

To give some flavor of the spatially localized surface chemical information that can be obtained from SEHI, we give some examples on powders used in additive manufacturing and LIB cathodes. As surface chemical characterization results could be influenced by specimen preparation, we present suitable methods for the preparation of pristine powders.

5.1. Powder preparation and evaluation

5.1.1. Test materials

CarbonMide® (CM) (EOS, Munich, Germany) is a commercial additive manufacturing powder feedstock used in selective laser sintering (SLS) to form a composite of carbon fiber (CF) in a polyamide (PA)– 12 matrix (Jansson and Pejryd, 2016). PA, also named nylon, is a polymer and 12 denotes the number of carbon atoms in the repeat unit which is shown in Fig. 9. A wide range of additives, increasingly in the form of nanomaterials such carbon black (CB), are used to adapt the powder properties to the laser sintering process or the resulting part properties (Hupfeld et al., 2018). PA-12 – CF (70:30 wt%) composite SLS parts had a flexural strength 57% higher than those made from pure PA-12 (Yan et al., 2011). CM has been chosen as a test material for powder-SEHI as CFs and PA-12 particles are easily differentiated in SEM images owing to morphology: CF is a high aspect ratio cylinder whereas PA-12 particles are randomly ellipsoidal. PA-12 is an insulator and thus causes challenges for SEM analysis. SE spectroscopy studies of carbon allotropes have developed an understanding of the characteristic SE spectrum shape from sp^2, sp^3 and amorphous hydrogenated (*a-CH*) carbon bonding (Lu et al., 2021; Abrams et al., 2019; Willis et al., 1972).

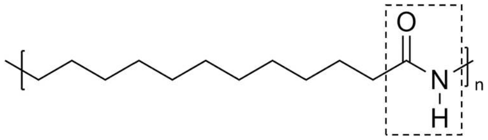

Fig. 9. Polyamide-12 (nylon 12, PA-12) repeat unit. 12 denotes the number of carbon atoms in the repeat unit. The amide group is within the dashed line.

Surface chemical analysis of the CFs in the feedstock is valuable in light of efforts to improve the adhesion between CF and the PA-12 matrix by surface functionalisation of CF. For instance, plasma treatment can produce oxygen functionalities on the surface of CF resulting in improved adhesion to a PA-12 matrix (Erden et al., 2010). Targeted surface oxidation followed by coating of CFs with PA-12 prior to SLS improved the mechanical properties of fabricated parts versus those made from untreated and mechanically mixed CF/PA-12 (Yan et al., 2011). Equally, plasma treatment has been suggested to modify the surface of the PA-12 powder, resulting in notable changes in wettability (Almansoori et al., 2018). Thus, surface chemical analysis of polymer powders is of interest too but has not been carried so far, due to the challenges related to insulating powders (see Section 4.3). However, SEHI has been applied in the surface chemical analysis of plasma treated biopolymers and SE energy windows sensitive to CH, OH and CO surface functionalities were identified and used to map relevant variation of these functional groups across the surface (Farr et al., 2020).

A second powder material system of substantial interest are lithium nickel manganese cobalt oxides used as active cathode material in LIBs. The specific example investigated here are powders (with the formula $Li(Ni_{0.8}Mn_{0.1}Co_{0.1})O_2$, (NMC811 from Targray) and $Li(Ni_{0.6}Mn_{0.2}Co_{0.2})O_2$ (NMC622 from BSAF). Substitution of cobalt for nickel (roughly half the cost of cobalt) has increased the specific capacity of cathode material in the $Li(Ni_{1-x-y}Mn_xCo_y)O_2$ (NMC) family from 160 $mAhg^{-1}$ (NMC111) to ~200 mAh g^{-1} (NMC811) (Jun et al., 2017). The material should be handled carefully to maintain a pristine surface, since the surface will react with air and moisture to produce residual lithium compounds of Li_2CO_3 and LiOH (Busà et al., 2021). Residual lithium compounds create a range of problems from poor electrode slurry characteristics, to consumption of the initial lithium inventory, to accelerated electrolyte degradation during cell cycling (Seong et al., 2020; Kim et al., 2018; Grenier et al., 2017). Here, we elect to handle NMC811 in an argon-filled glovebox to observe the surface condition at the point it is included in the electrode slurry for LIB cathode casting. An application condition slurry cast LIB cathode is prepared with the NMC622.

Where reference SE spectra are unavailable, as in the case of the NMC material, material regions within the SEHI field of view (FOV) may be interpreted to give spatially localized qualitative information about order/disorder and work function based on observations in other materials systems. For example, the extent of ordering in organic materials (carbon allotropes) and organic-inorganic hybrid perovskite materials has been shown to be reflected in SE spectra in peak broadening (Lu et al., 2021; Kumar et al., 2017). In the LIB cathode slurry cast cathode, functional groups such as CH_x present in polyvinylidene fluoride (PVDF, Fig. 10) and carbon black (CB) have associated SE spectrum energy ranges identified in other studies (Farr et al., 2020; Abrams et al., 2019).

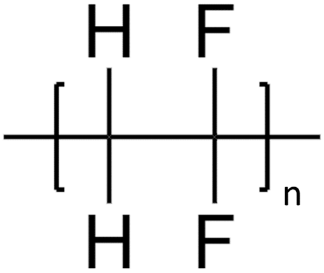

Fig. 10. Polyvinylidene fluoride (PVDF) polymer repeat unit. PVDF has CH and C-F functionalities. PVDF is used as a polymer binder in LIB cathodes.

5.1.2. *Field's metal SEHI specimen preparation*

Field's metal (Alfa Aesar) is a eutectic alloy of 32.5 wt% Bi: 51 wt% In: 16.5 wt% Sn. 0.5 g Field's metal was placed in a crucible cut from a 108 cell silicon mold for making tablets with cells 15 mm in diameter (for 12.5 mm dia. SEM stub) and 150 mm deep. The crucible with foil lid was placed on a hotplate set to 85 °C (Fig. 11a). Aluminum 12.5 mm diameter grooved SEM stubs were also placed on the hotplate for preheating. Meanwhile, powder was transferred from stock to the mold using a 10 μL pipette with disposable tips resulting in < 0.5 mg of powder in the mold. The mold was agitated to distribute the powder. The mold was placed on the same hotplate set at 85 °C for preheating. Using SEM stub grippers, the now molten Field's metal was poured from the crucible into the mold. The droplet of molten Field's metal was swilled around the preheated mold to cover it with powder. The mold was removed from the hotplate and the preheated SEM stub was gently pressed onto the Field's metal droplet. After the Field's metal had solidified, the SEM stubs with Field's metal were removed from the silicone mold and put in holders. A blower (handheld in the glovebox) was then used to remove any excess powder.

5.1.3. *LIB NMC622 slurry cast cathode*

To make the NMC622 cathode representative in this work, we follow a typical electrode manufacturing formula. The weight ratio between NMC622 (active material), PVDF (binder), and conductive CB additive was 96: 2: 2. All powders were dried in a vacuum oven at 120 ℃ overnight to remove moisture, then mixed in N-methyl pyrrolidone (NMP) solvent to form a homogenous slurry. The cathode slurry was coated on a piece of aluminum foil via a doctor blade thin-film applicator with a 300 μm setting thickness. The coated wet electrode was subsequently dried at 100 ℃ to remove NMP solvent and to form a dry electrode with a thickness of about 100 μm. Then the electrode was punched into 15 mm disks via an electrode punching machine.

5.1.4. *Cold pressed pellet*

CarbonMide® (CM), polyvinylidene difluoride (PVDF) and carbon black (CB) were ground together in a 4:4:2 wt ratio to make a 15 mg pellet of 10 mm diameter. Powders with static charge, such as carbon black, were 'fluffed' after weighing with an edge of foil to break up large agglomerations. The powder was poured into the pellet die and pressed with 1.5 tons pressure for 30 s using a hydraulic press (Specac). The pressed pellet was then slid out of the die and fixed to an aluminum stub with an adhesive carbon tab. Hydraulic pressing can be done as part of a glovebox preparation by transferring the pellet die out of the glovebox in an argon filled sealed plastic bag for pressing before continuing the preparation in the glovebox.

5.1.5. *Carbon tab*

A 10 μL pipette was used to transfer < 0.5 mg powder to a glass slide. The powder was further dispersed on the glass slide by lightly tapping the slide at an angle. A visual check of even contrast in the powder region made by holding the glass slide on a white background was made to confirm the uniformity of the powder layer. An SEM stub with an adhesive carbon tab was then pressed lightly onto the glass slide to transfer the powder layer from the glass slide.

5.1.6. *Adhesion and charging evaluation*

Prior to insertion into the SEM, powder preparations were blown with gas, either with a compressed air hose or a handheld blower in the glovebox. Specimens were then evaluated using an optical microscope with horizontal field width (HFW) of 730 μm at random points to check for particle clusters.

LV-SEM imaging was carried out in the FEI Nova NanoSEM 450 with a beam voltage of 1 kV and ETD. The scanning pattern used was 8 interlace with a dwell time of 100 ns. The evaluation of particle grounding contact with the substrate/embedding media was made by increasing the magnification of an area while imaging with the ETD until a typical HFW for SEHI was reached (HFW < 80 μm). Increases in magnification (and also in electron dose) were abandoned if there was evidence of specimen charging as in Fig. 12 where the bright portion of the image top center is indicative of localized build up of charge.

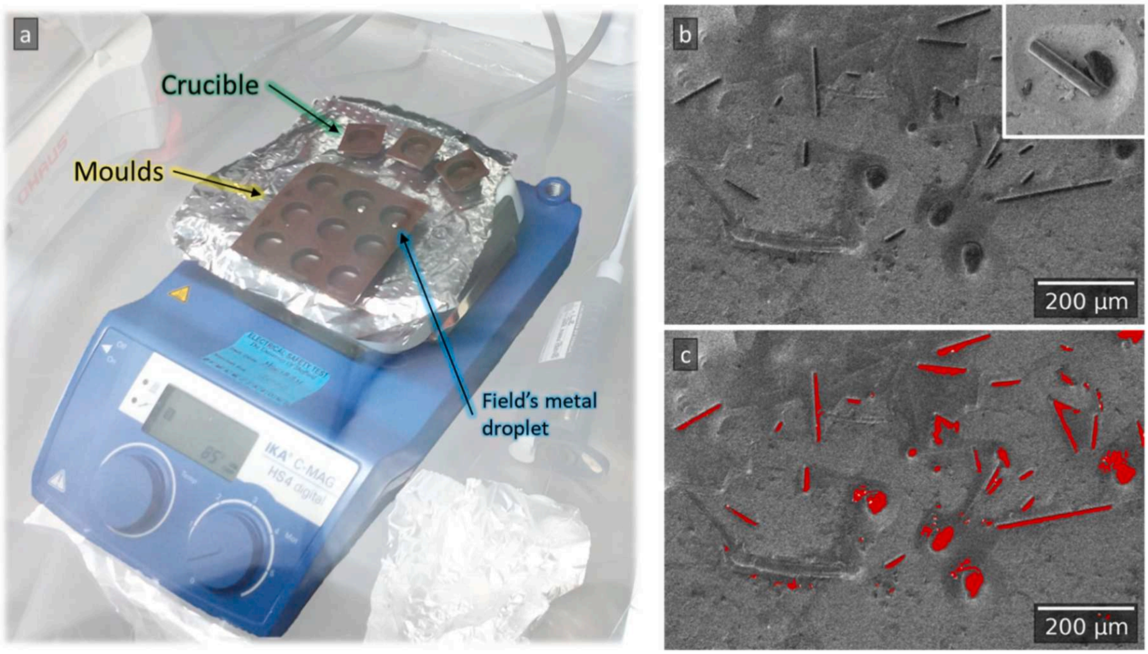

Fig. 11. Field's metal preparation of CarbonMide® (CM) additive manufacturing powder feedstock composed of carbon fiber (CF) and polyamide-12 (PA-12). (a) hotplate and dimpled silicone mold for Field's metal specimen preparations set up in the glovebox. (b) good powder dispersion and adhesion is achieved by swilling the molten Field's metal droplet around a powder filled mold, enabling CF and PA-12 to be imaged at higher magnifications (inset horizontal field width 75 μm). (c) the contrast of the Field's metal embedding media is such that rudimentary segmentation of particles in the powder sample is possible by binarizing the image.

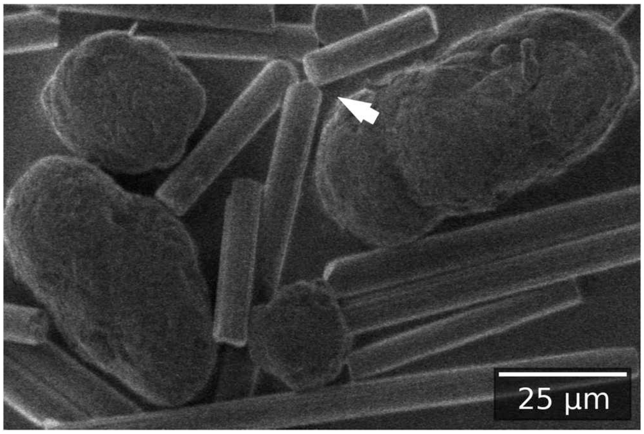

Fig. 12. CarbonMide® (CM) on a carbon tab at a HFW of 124 µm showing inconsistent materials contrast and a bright region at the top center of the image indicative of localized specimen charging (arrow).

5.2. *Energy calibration and SEM chamber cleaning*

The mirror/deflector electrode (see Section 4.2 for description) determines the maximum energy of the detected SEs. A calibration curve can be obtained by systematically changing the stage bias and recording the shift in the S-curves, as first described by Kazemian et al. when by varying the potentials at the deflector electrode (Kazemian et al., 2007). Fig. 13a and b show results obtained in a similar stage bias experiment when an S-curve is collected by applying different potentials to the mirror electrode, as expressed in mirror voltage (MV). First the S-curve is obtained (Fig. 13a) by plotting the average gray value in images collected at different MV without a stage bias. Further S-curves are collected for a range of stage bias settings. Then the MV at the maximum gradient of the S-curve is obtained for each stage bias (Fig. 13a). This is to reflect the shift of the spectrum resulting from the applied stage bias while avoiding uncertainties resulting from the slow onset of the S-curves. Energy shift equivalent (E), the energy shift expected from the application of the stage bias, (described in Section 4.2) is plotted against the MV at the maximum gradient of the S-curve (Fig. 13). A linear fit results in $E[\mathrm{eV}] = -0.3927[\mathrm{eV/V}]\times\mathrm{MV}[\mathrm{V}]+ 3.052[\mathrm{eV}]$ where units are in square brackets. To align the spectrum we adjust the constant by comparison to reported SE peak positions for highly oriented pyrolytic graphite (HOPG). SE spectra collected from HOPG are checked against, for example, the sp^2 and sp^3 peaks in spectra from fresh, aged and EBID condition HOPG as demonstrated in Figs. 13c and 13d. These steps yield an energy calibration of $E[\mathrm{eV}] = -0.3927[\mathrm{eV/V}]\times\mathrm{MV}[\mathrm{V}]+ 6[\mathrm{eV}]$. Fig. 13e summarizes the steps used in the calibration procedure.

Previous SEHI studies have measured the surface chemistry in regions of EBID on HOPG and Ti alloy (Farr et al., 2021; Abrams et al., 2019). In regions of EBID of SEM chamber contamination on HOPG, Abrams et al. show increased emissions at 4.5–6 eV attributed to sp^3-like carbon while Farr et al. show increased emissions at 2–4 eV attributed to amorphous carbon. The exact EBID species is likely to vary with chamber contamination, which in turn depends on many aspects of SEM operation: the specimen loading procedure; FIB usage; chamber cleaning procedures; the specimens themselves (Asahina et al., 2015; Michael, 2011). Although the influence of chamber contamination on EBID is beyond the scope of this article, some aspects can be explained simply. The thickness of the deposited contamination layer is related to electron dose (Vladár and Postek, 2005), and Abrams et al. show that it is not uniform across the scan area, with the thickest layer to the left of the scan area up to ~100 nm for a 146 Cm^{-2} electron dose (Abrams et al., 2019). Jepson et al. observed a ~3 nm deposition layer on silicon in the scan area which received an electron dose of 22.1 Cm^{-2} (Jepson et al., 2010). The influence of the electron dose on the shape of the SE spectrum of HOPG is shown in Fig. 14a. The electron dose applied during SEHI collection, D_{spec} [Cm^{-2}], can be quantified by Eq. 1 from Stehling (Stehling, 2020) modified to include scan interlacing,

$$D_{spec} = \frac{I_0 \times t_{dwell} \times n_{px} \times n_{avg} \times n_{spec}}{A \times l_{intl}} \qquad \text{(Eq. 1)}$$

where I_0 is the beam current, t_{dwell} is the dwell time, n_{px} is the number of pixels, n_{avg} is the number of scan averages, n_{spec} is the number of images in the spectrum, A is the image area and l_{intl} is the line interlacing. Fig. 14a shows the SE peak centered at 2.2 eV related to contamination increases in intensity with D_{spec}, which is cumulated either by serial acquisition in the same area or reducing the HFW. The peak intensity is plotted against D_{spec} to show the cumulative relationship (Fig. 14b).

Methods to manage EBID and chamber contamination have been proposed in the fields of ion beam fabrication and LV-SEM. Farr et al. apply a plasma FIB Xenon ion etch to a Ti6246 alloy and observed the reduction in amorphous carbon contamination when using SEHI (Farr et al., 2021) as can be seen in Fig. 15a. An alternative approach is the use of a lower primary beam energy to remove contamination. Mikmeková et al. show carbon desorption and deposition on graphene depending on the PE energy. Desorption of carbon contamination on graphene occurred when exposed to PEs with an energy of 500 eV, whereas 5 keV PEs resulted in deposition of carbon contamination (Mikmeková et al., 2020) (see Fig. 15b).

5.3. *Instrument parameters*

Important instrument parameters for SEHI as carried out in this work are listed in the Table 3. Control and reporting of these parameters facilitates the comparison between SEHI data volumes and reproducibility. The Targray NMC811 dataset was collected with the FEI Helios Nanolab 660/G3 dual beam microscope (Helios Nanolab) with Elstar column, the BSAF NMC622 with FEI Helios G4 PFIB CXe dual beam microscope (Helios PFIB) with Elstar column and the CarbonMide® dataset was collected with the FEI Nova NanoSEM 450 (Nova). The parameter classes and labels in Table 1 are taken from the FEI metadata scheme which records 20 parameters and 163 labels in raw image metadata for the Helios Nanolab.

TLD brightness is kept constant between datasets to include the noise floor when live imaging. Contrast was optimized manually for each dataset with the aim to use the maximum range of gray values without clipping the image gray level histogram. Images collected in the Helios Nanolab and Helios PFIB were 8-bit format (256 gray levels).

The NMC622 dataset collected with the Helios PFIB. Scan interlacing was 1, working distance was 4.1 mm, TLD brightness was 35.5096. All other parameters listed in Table 3 were the same. The CarbonMide® dataset collected with the Nova used the same Beam and Vacuum parameters. The lens mode was set to immersion. Scan interlacing was 8, dwell time was 100 ns, scan integration was 16 frames, extractor tube voltage was + 250 V. Working distance was 4.0 mm. TLD brightness was set to 45.7. There is no beam current information available for the Nova. Images were 16-bit (65,536 gray levels). SE spectra were collected over the range 0–5.99 eV with energy step of 0.176 eV. The settings of MV in the Helios Nanolab are equivalent to − 2.0–7.2 eV with 0.24 eV energy step. In both cases, detector gain remained constant throughout the image acquisition series and was set to optimize contrast in the image taken at the final deflector voltage.

5.4. *Data processing*

A template matching algorithm using a region from the final image was used to align features in the SEHI data volume. Average images are produced by averaging pixel values per pixel location in the SEHI data volume. Regions of interest (ROIs) were identified manually or by thresholding pixel values in the average image. An approach outlined in

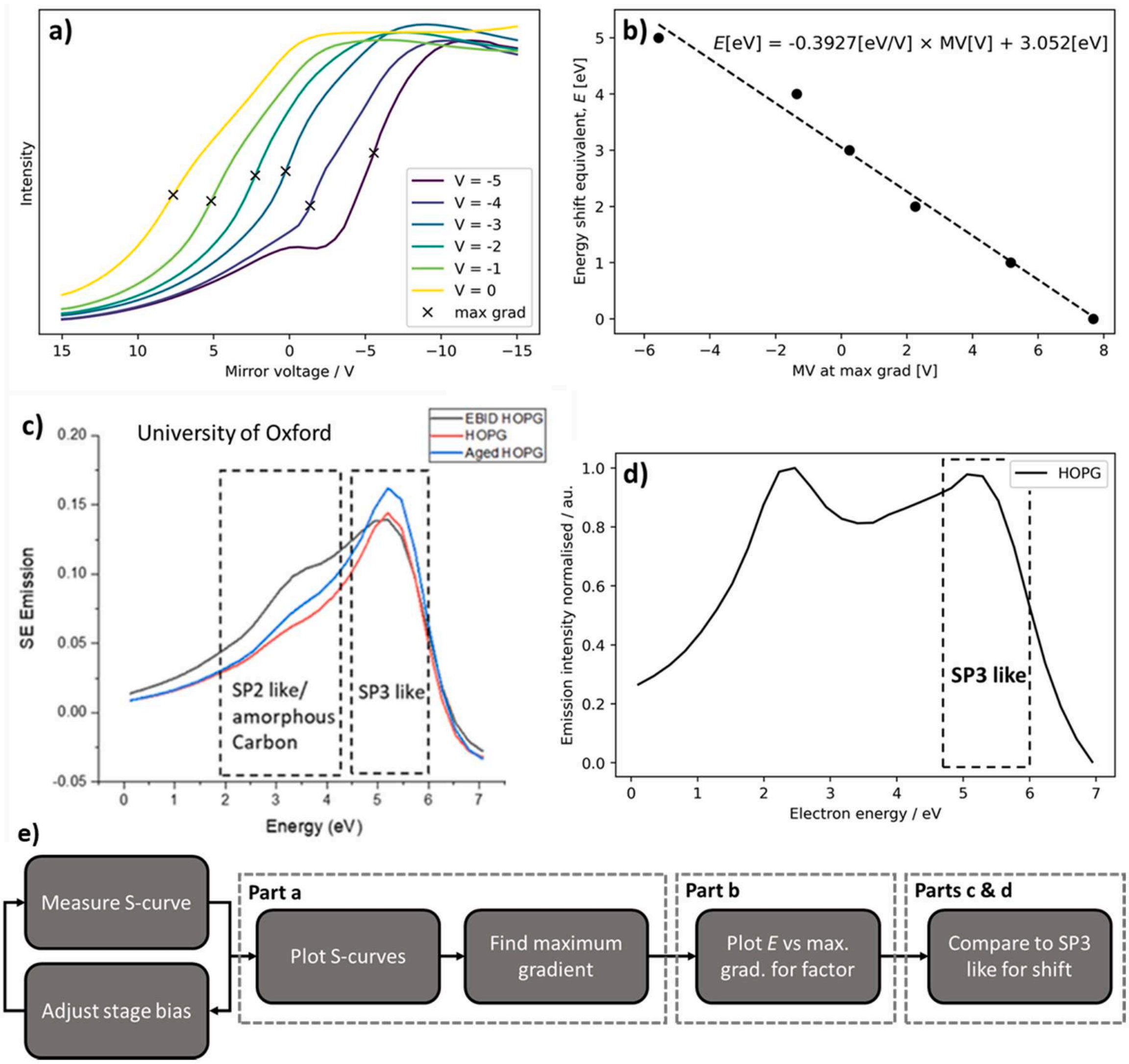

Fig. 13. approach to energy calibration for SE energy spectroscopy. (a) experimental S-curves taken at stage bias voltages with points of maximum gradient. (b) Plot of energy shift equivalent, E [eV] versus MV at maximum gradient [V] yields the linear line of best fit. (c and d) The shift is found by comparing known SE emission peaks. (c) SE spectrum adapted by cropping from Farr *et al.*, "Monitoring Carbon in Electron and Ion Beam Deposition within FIB-SEM" (Farr et al., 2021) under CC BY 4.0 license (https://creativecommons.org/licenses/by/4.0/legalcode). The sp^3-like carbon associated peak centered at 5.2 eV in the provides an absolute shift of + 6 for the HOPG spectrum in (d). The SE emission peak centered 2.2 eV is associated with electron beam induced deposition of chamber contamination. The conversion of MV to equivalent electron energy is thus $E[\mathrm{eV}] = -0.3927[\mathrm{eV/V}](\mathrm{MV}[\mathrm{V}]) + 6[\mathrm{eV}]$. (e) Flow diagram summarizing the energy calibration approach presented in parts (a-d).

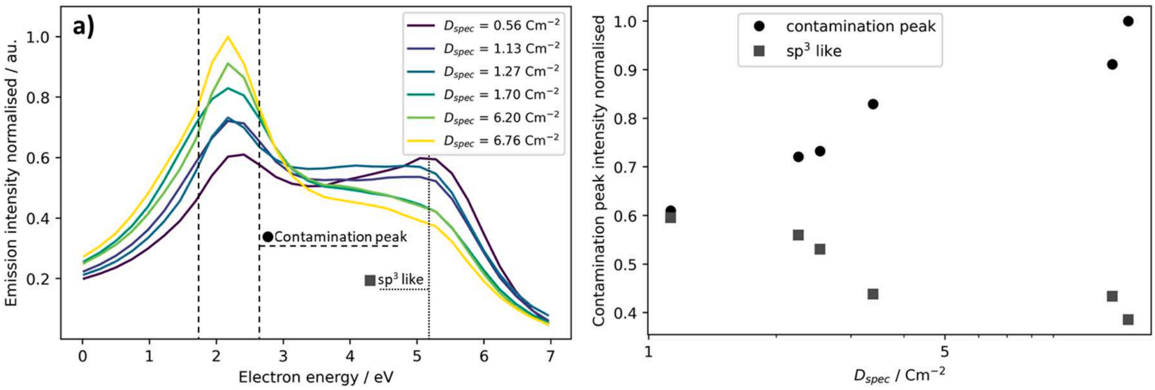

Fig. 14. (a) SE spectra from HOPG with the 2.2 eV peak associated with electron beam induced deposition (EBID) of chamber contamination within the dashed outline and sp^3-like carbon labeled at 5.2 eV. (b) Contamination peak intensity and sp^3-like carbon intensity versus D_{spec} showing the ratio of contamination: sp^3-like carbon intensity increases with electron dose.

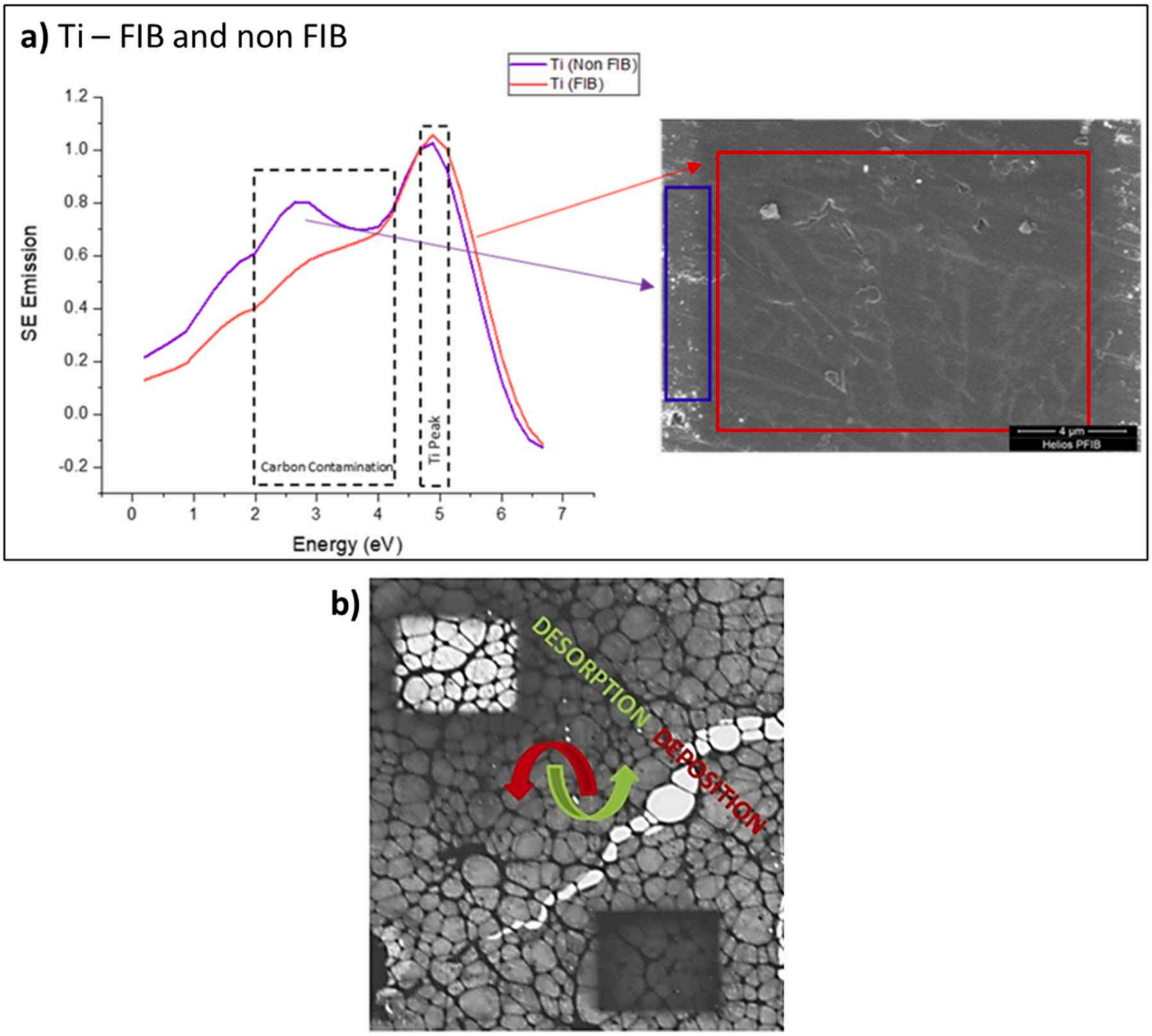

Fig. 15. (a) Plasma Xe FIB etch, 30 kV; 1 nA; 20 s (D_{etch}, 0.2 nC μm^{-2}), cleans carbonaceous contaminants from a Ti6246 alloy surface as evidenced by the decrease in 2–4 eV emissions. Adapted by cropping from Farr *et al.*, "Monitoring Carbon in Electron and Ion Beam Deposition within FIB-SEM" (Farr et al., 2021) under CC BY 4.0 license (https://creativecommons.org/licenses/by/4.0/legalcode). (b) STEM image of graphene with areas of carbon desorption (top left) and deposition (bottom right) by irradiation with 500 eV and 5 keV electrons respectively, from Mikmekova, "Low-energy electron microscopy of graphene outside UHV: electron-induced removal of PMMA residues used for graphene transfer" (Mikmeková et al., 2020) under CC BY 4.0 license (https://creativecommons.org/licenses/by/4.0/legalcode).

Table 3
Parameters for collection of Targray NMC811 datasets in this work by the Helios Nanolab 660/G3 dual beam microscope with Elstar column.

Parameter class	Parameter label	Relevance	Setting in this work
Beam	HV	See LV-SEMSection 2.1	1000 V
EBeam	BeamCurrent	See LV-SEMSection 2.1	50 pA
	LensMode	See LV-SEMSection 2.1	Immersion
EScan	Dwell	D_{spec} input (Eq. 1)	50 ns
	ScanInterlacing	D_{spec} input (Eq. 1)	8
Image	ResolutionX	D_{spec} input (Eq. 1)	1536
	ResolutionY	D_{spec} input (Eq. 1)	1024
Scan	Average	D_{spec} input (Eq. 1)	32 frames
Stage	WorkingDistance	Influences: immersion lens (Section 2.1); extractor/suction field (Section 4.2)	3.9 mm
TLD	SuctionTube	SeeSection 4.2	150 V
	Mirror	SeeSection 4.2	Start 20.4 V, Stop − 3 V, Step: − 0.6 V
	Brightness	Set to include live image noise floor	41.3071
Vacuum	ChPressure	Influences contamination and EBID (Section 5.2)	~ 5E-04 Pa

Fig. 16 was used to plot SE spectra from ROIs. The SEHI data volume (represented by the average image in Fig. 16a) was blurred in x and y using a uniform box blur filter (Fig. 16b). The uniform filter reduces noise in the image series and the size of the box used for filtering limits the spatial resolution of the images and thus the spatial localization of SE spectra. The pixel value along the z-axis is plotted per pixel location in the ROI (Fig. 16c) to give the z-axis profile (S-curve). The S-curve is differentiated produce an SE spectrum for each the pixel location (Fig. 16d). Spectra are normalized to the maximum of the SE spectrum obtained from whole field of view (FOV) to show relative emission intensities. The SE spectrum of the ROI is derived by averaging spectra at each pixel location within the ROI and the error bars represent the standard deviation of pixel location spectra within the ROI (Fig. 16e). The SE emission intensity (y-axis in Figs. 16d and 16e) is related to change in pixel gray value which is related to the counts received by the SE detection system.

5.5. *Examples*

SEHI is applied to the characterization of powder materials from additive manufacturing and energy storage applications. Test materials, CarbonMide® (CM) and NMC LIB cathode material, are described in

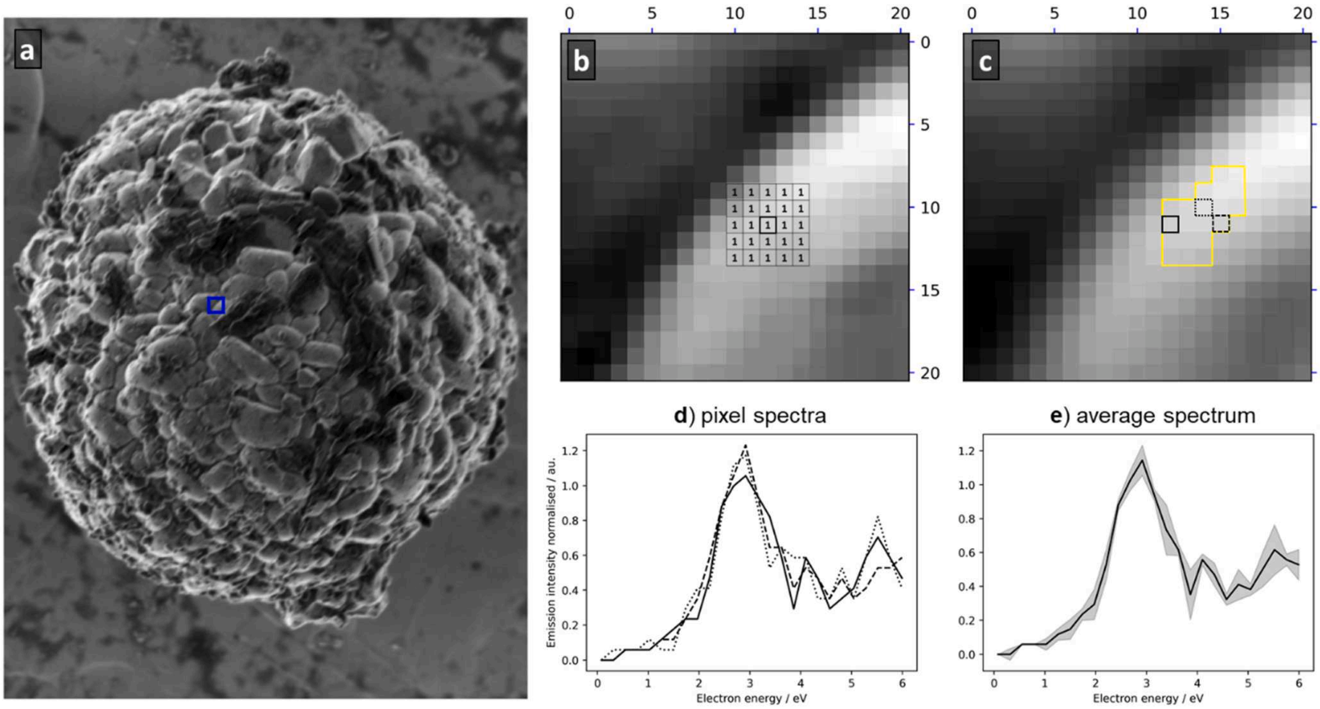

Fig. 16. (a) average image with horizontal field width of 8.48 μm. The blue square outlines the 20 × 20 pixel region shown in (b). (b) The value of each pixel becomes the average of pixel values in a surrounding 5 × 5 pixel box. It is a uniform box blur as each pixel in the box has equal weighting. In this case the box width is 55 nm. (c) Blurred image in the region of (b) with a region of interest (ROI) outlined in yellow. (d) Pixel spectra corresponding to outlined pixels in the ROI in (c). e) Average of pixel spectra in (d) with the standard deviation of pixel spectra filled in gray.

detail in Section 5.1.1. Although examples are limited to two example material systems, carbonaceous, polymer and metal oxide components are present. The examples represent the potential for application of SEHI for powder characterization in other application areas.

5.5.1. AM polymer composite

SEHI was conducted on CM prepared in a pellet sample (described in Section 5.1.3). Since the CM component morphologies are easily identifiable, SE spectra are plotted from CF, PA-12 and binder regions outlined in Fig. 17a. The respective SE spectra are shown in Fig. 17b and overlayed with the energy regions dominated by specific functional groups as reported in previous studies. SE peaks reported previously from HOPG (Abrams et al., 2019) and polymer (Farr et al., 2020, 2019) surfaces have been associated with sp^2 carbon, polymer molecular order, CHx groups, -OH group and $C{=}O$ groups to the energy ranges of 2.0–3.3 eV, 1.4–2.3 eV, 2.9–4.3 eV, 4.3–5.0 eV and 5.0–5.5 eV, respectively. In the region labeled C 1 s, SE spectra from the ROI located in CF, PA-12 and binder respectively, are distinct (the standard deviation does not overlap) showing that these carbon-based materials can be differentiated by their SE spectra in this energy range. Materials can also be differentiated in the sp^2 region. The ROI located on the CF surface exhibits a peak (centered at 2.3 eV). The SE emission intensity from PA-12 and binder (PVDF+CB) materials in this energy range are much lower. Furthermore, Figs. 17d and 17e show that the SE emission spectrum in the range of the sp^2 carbon peak from a ‘clean’ CF surface and a surface on the same fiber visibly contaminated with binder material, show distinctly less of sp^2 carbon in the contaminated region. Both cases (a and b; c and d) in Fig. 17 demonstrate the ability of SEHI to provide information about the difference in bonding present at carbonaceous material surfaces, including a CF surface contaminated with particles 60–200 nm in diameter, demonstrating the surface sensitivity of the technique. This information is not available in the elemental analyses of materials by EDX or BSE analyses in the SEM as reviewed in Sections 2.2 and 2.3.

Despite being used to identify the chemistry of CF surfaces with distinct SE spectra from PA-12 and binder regions, the pressed pellet preparation imposes limitations on the chemical and morphological analysis of powders by SEHI. Firstly, contamination of powder surfaces by CB and PVDF occurs, which obscures the chemical difference of the underlying material as demonstrated by the SE spectra from CF and PA-12 particle surfaces with regions of PVDF adhesion (highlighted in Fig. 17d and SE spectra in Fig. 17e). Secondly, pressing causes soft powders to coalesce and transfers the surface topography of the die to the pellet (Fig. 18) so that the original powder morphology is destroyed, invalidating particle shape, size and morphology measurements.

5.5.2. LIB cathode active material powder

Images of the pristine NMC811 secondary particles, made up of assembled aggregates of primary particles, embedded in Field’s metal show high contrast between populations of dark and light material on the surfaces the of the particles (Fig. 19ai and 19c). This dark material displays evidence of two morphologies. Figure 19a shows dark particles, smaller in diameter than the primary particles, found distributed on the primary particle surface. Fig. 19c shows a different arrangement, where the right-hand particle in the figure appears to have a uniform covering of the darker material with a loss of definition between primary particles. SE spectra (Figs. 19b and 19d) normalized to the field of view (FOV) originating from these dark material morphologies are compared to SE spectra originating from lighter material regions in the same FOV (the regions from which SE spectra are obtained are described in Fig. 19aii and 19c). SE spectra in Fig. 19c were obtained from the dark particles separated by thresholding a region on the top of the secondary particle (labeled ‘Dark thresh.’ and filled in blue Fig. 19aii) and the inverse of this region is composed of lighter material. SE spectra in Fig. 19d are plotted from the top surface of the secondary particles in Fig. 19c named ‘light’ (left-hand particle) and ‘dark’ (right-hand particle). The spectra in Figs. 19b and 19d were normalized to the maximum emission intensity in the range 0–6 eV within the FOV.

One explanation for material in an SE image to appear dark is that the material is positively charging during imaging – where the emitted

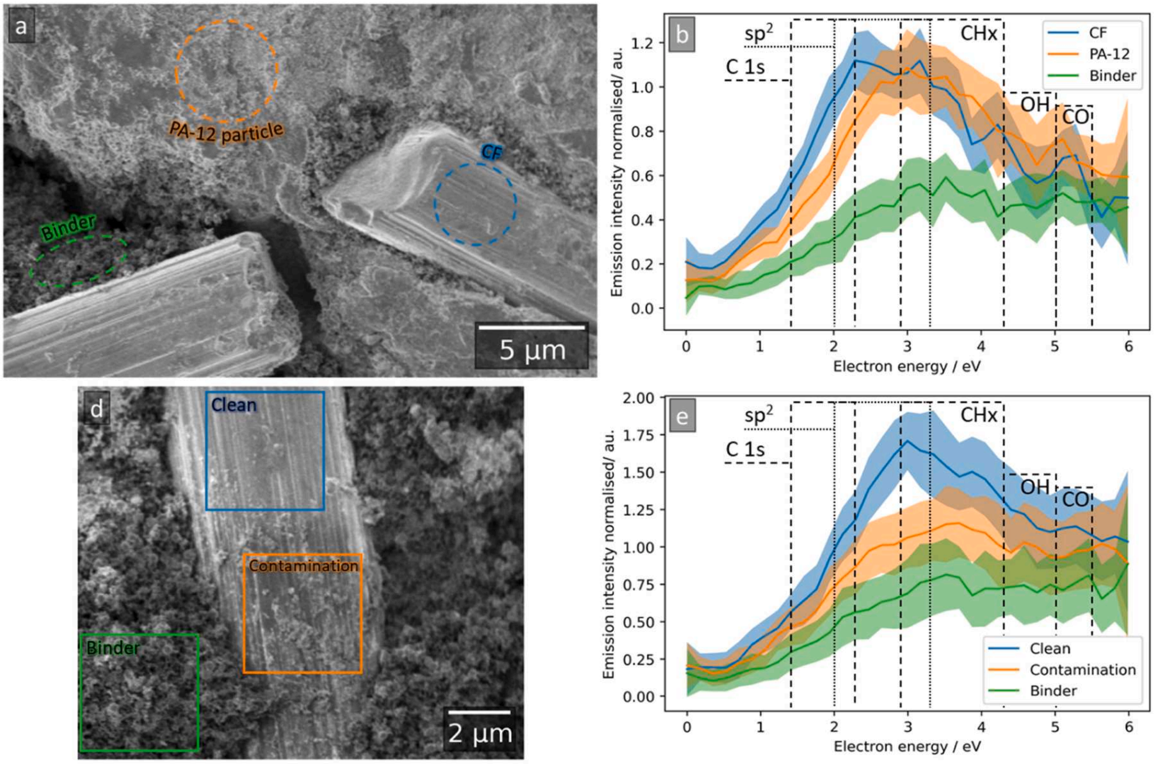

Fig. 17. (a and d) images of CarbonMide® additive manufacturing powder feedstock composed of carbon fibers (CF) and polyamide-12 (PA-12) particles prepared in a pressed pellet with polyvinylidene difluoride (PVDF) and carbon black (CB) in a 4:4:2 ratio of weights. (a) Annotated regions are descriptive regions of interest (ROIs) of PA-12 particle, CF and PVDF+CB binder from which part (b) secondary electron (SE) spectra are plotted showing chemically distinct SE emission intensities in the C 1 s and sp^2 carbon energy ranges. (d) image of CF in binder with ROIs from which spectra in part (e) are plotted. The SE spectra in (b and e) are normalized to the field of view (FOV) maximum emission intensity. Error bars in SE spectra plots (b and e) are ± the standard deviation (SD) of pixel SE spectra in the ROI from which the average spectra are calculated (solid lines). The spectral spatial resolution equivalent to 875 nm and 547 nm in parts (a) and (b) respectively. Emission ranges of interest are 2.0–3.3 eV for sp^2 bonded carbon from (Abrams et al., 2019) and 1.4–2.3 eV from (Farr et al., 2019), 2.9–4.3 eV, 4.3–5.0 eV and 5.0–5.5 eV for CHx, OH and CO groups respectively as identified in (Farr et al., 2020).

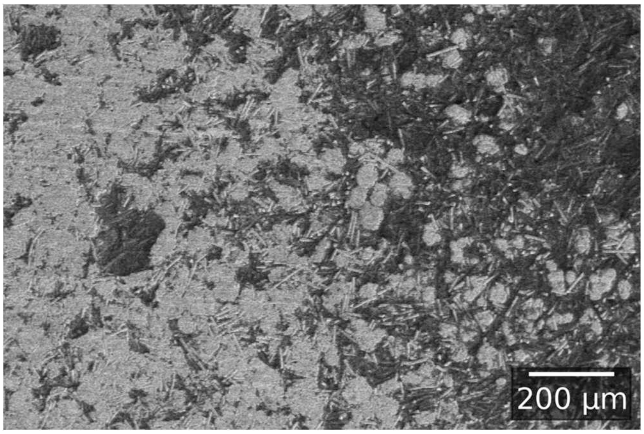

Fig. 18. destruction of powder morphology by cold pressing CarbonMide® into a pellet. Polyamide-12 (PA-12) particles coalesce and lose their original shapes (left). Die topography is transferred to the soft PA-12 material in the pellet visible as grooves (top left). Both changes to powder morphology invalidate shape and size measurements by SEM.

electron yield is above one – so that SE emissions are attracted back to the surface and go undetected (Postek and Vladár, 2015). However, this phenomenon is accompanied by a consistent shift in SE emission to lower energy from the positively charging region (Li et al., 2020), which is not observed in the SE spectra plotted in Figs. 19b and 19d. In fact, the SE spectra from ROIs within the same FOV show consistency in peak position above 2.5 eV. The first peak maxima in light regions appear at lower energy than for the dark material of both morphologies, which are higher by 0.24 eV and 0.60 eV respectively (Figs. 19b and 19d). There are several potential causes: a difference in pristine material surface composition, contamination species (resulting from air and moisture exposure, see residual lithium species in Section 5.1.1), material ordering or a combination of these. The higher onset observed in the spectra of the dark materials could be attributed to a higher surface energy barrier (work function, φ) for SE emissions. The same effect has been shown to produce contrast between contamination layers on HOPG surfaces imaged by energy-filtered (EF-) SEM, with amorphous hydrogenated carbon (*a*-CH) regions appearing brighter and regions of -OH surface functionalisation darker, due to reduced and increased φ respectively, versus the fresh HOPG surface (Abrams et al., 2019). In addition, the ‘dark’ SE spectrum in Fig. 19d shows broadening of peaks. Peak broadening in conjunction with reduced emission intensity in SE spectra was related to ordering of carbon allotropes (Lu et al., 2021). If this is also applicable to NMC materials, the right-hand particle in Fig. 19c and its spectrum in Fig. 19d could indicate the presence of a more disordered surface than the lighter left-hand particle. Thus, the SE spectra localized to dark and light regions show spectral features that suggest contrast is a result of variation in φ and that dark material morphology highlighted in Fig. 19c appears relatively more disordered compared to lighter left-hand particle in the same FOV. Determining the exact cause of the material contrast would require an in depth SEHI study of characterized reference materials rather than the commercial material.

Such in-depth studies are important as chemical variation at the surface of NMC material has a big impact on its electrochemical

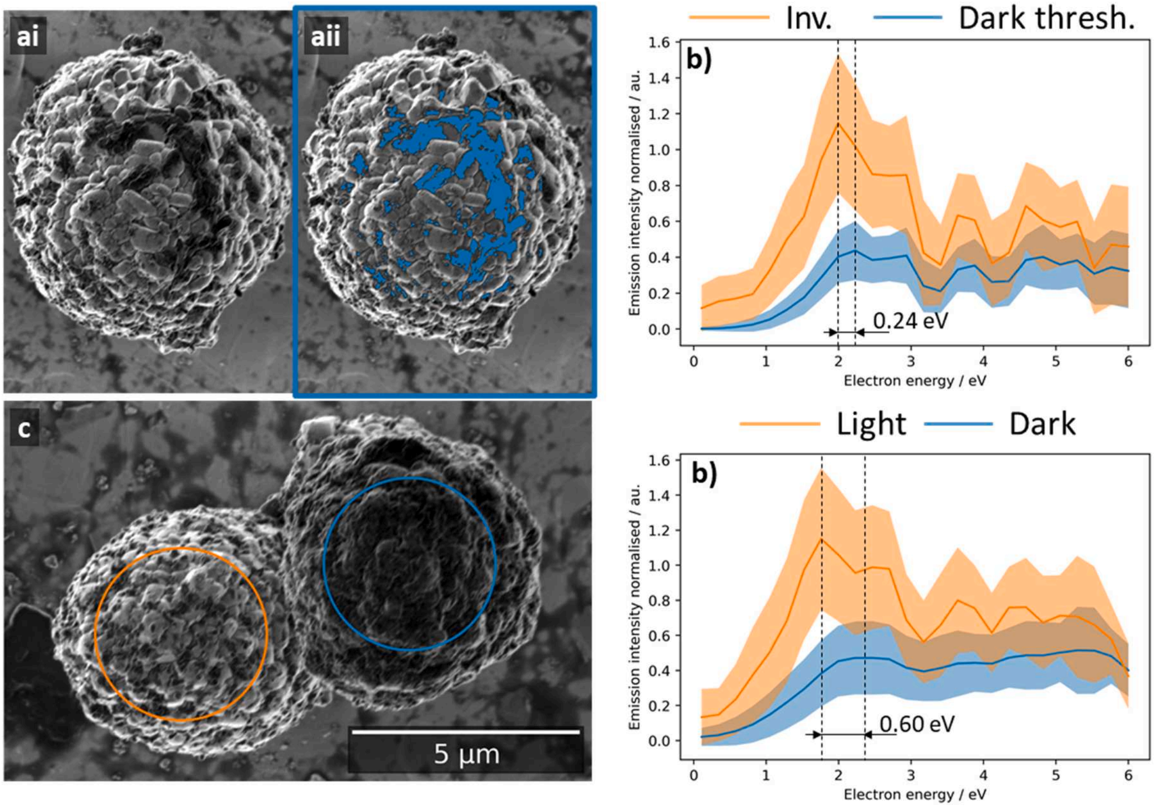

Fig. 19. a and c) Images of NMC811 secondary particles showing dark and light contrast between material on the NMC811 surface. Dark material has two morphologies: (a, box width 8.48 μm) particles smaller than the primary particle dispersed on the secondary particle surface, (c) right-hand particle uniformly darker and with loss of definition of primary particle boundaries. SE spectra (b) from the blue filled region (aii) separated by thresholding (labeled 'Dark thresh.') and its inverse ('Inv.') and SE spectra (d) from the 'light' left-hand particle and 'dark' right-hand particle circled in (c). Spectral energy resolution is 0.24 eV and the spatial resolution in (b) is 55 nm with a 5-pixel width box blur applied in x and y and (d) 89 nm with 8-pixel width box blur. The location of the first SE spectrum peak maximum for the dark material regions are 0.24 eV and 0.60 eV higher than that of the light regions in (b) and (d) respectively, while the peaks in light and dark regions are at the same energy above 2.5 eV.

performance. Approaches to engineer the NMC surface include surface treatments (Li_3PO_4, Al_2O_3 and YF_3 (Yan et al., 2018; Zhu et al., 2019; Chen et al., 2017)), concentration gradients and core-shell structures (Xu et al., 2019; Liao et al., 2016). Surface engineering has exposed particular powder surface chemistries to limit capacity fading (Xu et al., 2019; Liao et al., 2016); could reduce φ and therefore reduce the interfacial charge transfer resistance, electrolyte decomposition, and increase the lithium-ion diffusion (Chen et al., 2017). In all cases, a uniform coating is desirable to tailor and predict performance. Technology in surface treatment reaches the sub-nanometer scale (Yan et al., 2018; Zhu et al., 2019). Surface potential maps of NMC333 and YF_3-coated NMC333 have been obtained by Kelvin probe atomic force microscopy (KPAFM) (Chen et al., 2017). KPAFM was used to determine the average φ values for both materials, and maps to reveal the variation of the surface potential on a submicron scale. To meet the needs of the detecting at such a small scale, SEHI, with a spatial resolution of 55 nm,

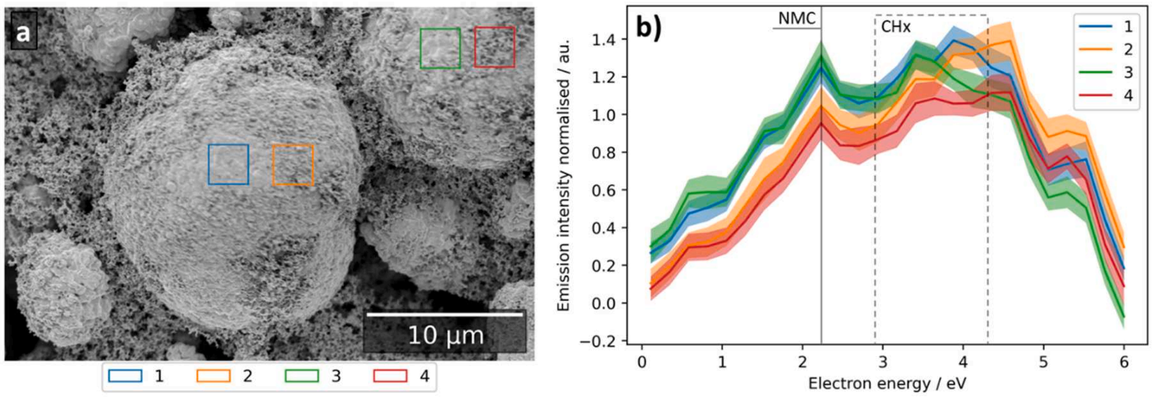

Fig. 20. (a) regions of interest (ROIs) from an NMC622 cathode from which spectra are plotted (b). (b) the secondary electron (SE) spectra from ROIs. The peak centered at 2.23 eV has been associated with NMC (this work) and the 2.9–4.3 eV range with CH_x (Farr et al., 2020) from the binder in this case. Emissions associated with NMC have distinctly higher intensity in regions 1 and 3 versus regions 2 and 4, indicating the extent to which NMC has been covered in the binder material. The applied uniform box blur width was 50 pixels giving a spatial resolution of 1.1 μm.

could achieve both spatially localized surface chemical characterization of sub-micron features on particle surfaces and relate these features to whole powder particles on the microscale.

The presence of localized differences at the pristine NMC811 particle surface shown above are likely to affect the electrochemical performance/and or lifetime of a LIB. The NMC622 was incorporated into a slurry cast LIB cathode to determine whether the pristine NMC surface was observable after cathode fabrication (Section 5.1.3). Fig. 20a displays the SE image of the slurry cast NMC622 LIB cathode. ROIs were plotted onto the spherical particles (Fig. 20a). Spectra were plotted from these ROIs (Fig. 20b). The spectra in Fig. 20b include an NMC associated peak centered at 2.23 eV and emissions 2.9–4.3 eV associated with CH_x groups (Farr et al., 2020). The CH_x groups originate from the PVDF polymer and CB in the binder material. At the NMC associated peak, spectra were divided into two distinct groups: SE spectra from ROIs 1 and 3 exhibit a more intense NMC peak than those obtained from ROIs 2 and 4 (Fig. 20b). This points towards to the presence of binder material on the surface of the NMC which was confirmed by visible nanostructured material in these ROIs. Although the absence of such nanostructures in ROIs 1 and 3 in Fig. 20a implies that in some areas a pristine surface is still accessible, the SE spectra exhibit much higher emissions associated with the CH_x group compared to NMC811 prepared in the Field's metal (Fig. 19). Thus, the presence of additional carbonaceous material from the slurry preparation is evident in SE spectra, even when not obvious from morphologies visible in the image. This result underlines the need for the Field's metal preparation method to observe the pristine powder surface. Comparing the pristine and slurry cast NMC materials serves as a practical example of the surface sensitivity of SEHI to surface chemistry modification in specimen preparation.

6. Conclusion and outlook

Spatially localized surface chemical characterization by SEHI has been trialed on three commercial powder materials: CarbonMide® additive manufacturing powder feedstock and air and moisture sensitive NMC811 and NMC622 LIB cathode active materials. Key to this was the Field's metal embedding method. It provides SEHI with consistent contrast between powder and embedding media for particle segmentation, preserves particle morphology, can be carried out inside a glovebox and does not contaminate powder surfaces with additional binder material. The adhesion and electrical grounding of the powder specimens prevented movement of the particles in the + 250 V extractor/ + 150 V suction fields necessary for SEHI.

SEHI extends the possibility of spatially localized surface chemical characterization to SEM instruments, once the preserve of SAM instruments with UHV conditions, due to a higher yield of SEs compared to AEs. The high yield of SEs enables low electron doses to be used to acquire SE spectra, and thus limit EBID in high-vacuum conditions. EBID has the potential to obscure powder surface chemical information. Here, understanding of the effects of surface contamination on the SE spectrum has not been fully investigated. The relation of surface contamination by EBID to electron dose was tracked by SE peak intensity in two energy regions. Position of contamination peaks in the SE spectra have varied between studies illustrating the importance to control chamber contamination. With the prerequisite of controlled chamber contamination conditions, SEHI has the capability to carry out localized surface chemical characterization. Bonding, order and work function of powder materials with a similar information volume to UHR LV-SEM imaging can be obtained from SEHI.

Declaration of Competing Interest

The authors declare that they have no known competing financial interests or personal relationships that could have appeared to influence the work reported in this paper.

Data availability

The datasets included in this article are available to download from 10.15131/shef.data.17081228 for use under CC BY-NC 4.0 license (https://creativecommons.org/licenses/by/4.0/legalcode).

Acknowledgments

C.R. thanks the Engineering and Physical Sciences Research Council (EPSRC) for funding under EP/N008065/1 and EP/V012126/1 and N.F. for fellowship (EP/T517835/1). S.C. acknowledges support from the EPSRC (EP/N001982/2). S.C. and J.N. acknowledge support from the Faraday Institution (grant number FIRG017). Y.S. acknowledges support from the Faraday Institution (grant number FIRG015). We thank Dr Nirmalesh Naveen for providing Targray NMC811 material. Electron microscopy was performed in the Sorby Center for Electron Microscopy at the University of Sheffield. The authors also wish to acknowledge the support of the Henry Royce Institute for J.N. through the Royce Equipment Access Scheme enabling access to the Plasma FIB facilities at Royce@Oxford; EPSRC (grant number EP/R00661X/1). G.M.H. and Y.S. acknowledge the use of characterization facilities within the David Cockayne Center for Electron Microscopy (DCCEM), Department of Materials, University of Oxford, alongside financial support provided by the Henry Royce Institute (grant number EP/R010145/1).

References

Abrams, K.J., et al., 2019. Making sense of complex carbon and metal/carbon systems by secondary electron hyperspectral imaging. Adv. Sci. 6 (19), 1900719 https://doi.org/10.1002/advs.201900719.

Almansoori, A., et al., 2018. Surface modification of the laser sintering standard powder polyamide 12 by plasma treatments. Plasma Process. Polym. 15 (7) https://doi.org/10.1002/ppap.201800032.

Asahina, S., et al., 2012. High-resolution low-voltage scanning electron microscope study of nanostructured materials. Microsc. Anal. 26 (7), 12–14.

Asahina, S., et al., 2014. Direct observation and analysis of york-shell materials using low-voltage high-resolution scanning electron microscopy: Nanometal-particles encapsulated in metal-oxide, carbon, and polymer. APL Mater. 2 (11) https://doi.org/10.1063/1.4902435.

Asahina, S., Sakuda, Y., Terasaki, O., 2015. Direct observation of nano-porous materials using low voltage high resolution SEM. Microsc. Microanal. 21 (S3), 27–28. https://doi.org/10.1017/s1431927615000938.

Baer, D.R., et al., 2010. Approaches to analyzing insulators with Auger electron spectroscopy: update and overview. J. Electron Spectrosc. Relat. Phenom. 176 (1–3), 80–94. https://doi.org/10.1016/j.elspec.2009.03.021.

Bell, D.C., Erdman, N., 2013. Low Voltage Electron Microscopy: Principles and Applications. John Wiley & Sons. https://doi.org/10.1002/9781118498514.

Billi, F., Benya, P., Ebramzadeh, E., Campbell, P., Chan, F., McKellop, H.A., 2009. Metal wear particles: what we know, what we do not know, and why. SAS J. 3 (4), 133–142. https://doi.org/10.1016/j.esas.2009.11.006.

Boyes, E.D., 1998. High-resolution and low-voltage SEM imaging and chemical microanalysis. Adv. Mater. 10 (15), 1277–1280, 10.1002/(SICI)1521-4095(199810)10:15<1277::AID-ADMA1277>3.0.CO;2-D.

Burgain, J., Petit, J., Scher, J., Rasch, R., Bhandari, B., Gaiani, C., 2017. Surface chemistry and microscopy of food powders. Prog. Surf. Sci. 92 (4), 409–429. https://doi.org/10.1016/j.progsurf.2017.07.002.

Burgess, S., Sagar, J., Holland, J., Li, X., Bauer, F., 2017. Ultra-low kV EDS – a new approach to improved spatial resolution, surface sensitivity, and light element compositional imaging and analysis in the SEM. Microsc. Today 25 (2), 20–29. https://doi.org/10.1017/s1551929517000013.

Busà, C., Belekoukia, M., Loveridge, M.J., 2021. The effects of ambient storage conditions on the structural and electrochemical properties of NMC-811 cathodes for Li-ion batteries. Electrochim. Acta 366. https://doi.org/10.1016/j.electacta.2020.137358.

Butler, J.H., Joy, D.C., Bradley, G.F., Krause, S.J., 1995. Low-voltage scanning electron microscopy of polymers. Polymer 36 (9), 1781–1790.

Chang, C.C., 1971. Auger electron spectroscopy. Surf. Sci. 25 (1), 53–79. https://doi.org/10.1016/0039-6028(71)90210-X.

Chen, L., et al., 2017. Enhanced electrochemical performances and thermal stability of LiNi1/3Co1/3Mn1/3O2 by surface modification with YF3. J. Alloy. Compd. 711, 462–472. https://doi.org/10.1016/j.jallcom.2017.03.130.

Chen, Q., et al., 2020. Imaging beam-sensitive materials by electron microscopy. Adv. Mater. 32 (16) https://doi.org/10.1002/adma.201907619.

Chung, M.S., Everhart, T.E., 1974. Simple calculation of energy distribution of low-energy secondary electrons emitted from metals under electron bombardment. J. Appl. Phys. 45 (2), 707–709. https://doi.org/10.1063/1.1663306.

Crouzier, L., Delvallée, A., Devoille, L., Artous, S., Saint-Antonin, F., Feltin, N., 2021. Influence of electron landing energy on the measurement of the dimensional properties of nanoparticle populations imaged by SEM. Ultramicroscopy 226. https://doi.org/10.1016/j.ultramic.2021.113300.

Demers, H., Brodusch, N., Woo, P., Gauvin, R., 2015. Origins and contrast of the electron signals at low accelerating voltage and with energy-filtering in the FE-SEM for high resolution imaging. Microsc. Microanal. 21 (S3), 705–706. https://doi.org/10.1017/s1431927615004328.

Egerton, R.F., Li, P., Malac, M., 2004. Radiation damage in the TEM and SEM. Micron 35 (6), 399–409. https://doi.org/10.1016/j.micron.2004.02.003.

el Gomati, M.M., Walker, C.G.H., Assa'd, A.M.D., ZadraŽil, M., 2008. Theory experiment comparison of the electron backscattering factor from solids at low electron energy (250–5,000 eV). Scanning 30 (1), 2–15. https://doi.org/10.1002/sca.20091.

Engelhard, M.H., Baer, D.R., Herrera-Gomez, A., Sherwood, P.M.A., 2020. Introductory guide to backgrounds in XPS spectra and their impact on determining peak intensities. J. Vac. Sci. Technol. A 38 (6), 063203. https://doi.org/10.1116/6.0000359.

Erden, S., Ho, K.K.C., Lamoriniere, S., Lee, A.F., Yildiz, H., Bismarck, A., 2010. Continuous atmospheric plasma oxidation of carbon fibres: influence on the fibre surface and bulk properties and adhesion to polyamide 12. Plasma Chem. Plasma Process. 30 (4), 471–487. https://doi.org/10.1007/s11090-010-9227-6.

Ernst, A.T., et al., 2020. Surface states of gas-atomized Al 6061 powders – effects of heat treatment. Appl. Surf. Sci. 534 https://doi.org/10.1016/j.apsusc.2020.147643.

Farr, N., et al., 2020. Understanding surface modifications induced via argon plasma treatment through secondary electron hyperspectral imaging. Adv. Sci. 1–5. https://doi.org/10.1002/advs.202003762 (2003762).

Farr, N., Pashneh-Tala, S., Stehling, N., Claeyssens, F., Green, N., Rodenburg, C., 2019. Characterizing cross-linking within polymeric biomaterials in the SEM by secondary electron hyperspectral imaging. Macromol. Rapid Commun. 41 (3) https://doi.org/10.1002/marc.201900484. E1900484 (1-8).

Farr, N.T.H., et al., 2021. A novel characterisation approach to reveal the mechano–chemical effects of oxidation and dynamic distension on polypropylene surgical mesh. RSC Adv. 11 (55), 34710–34723. https://doi.org/10.1039/D1RA05944K.

Farr, N.T.H., Hughes, G.M., Rodenburg, C., 2021. Monitoring carbon in electron and ion beam deposition within FIB-SEM. Materials 14 (11), 3034. https://doi.org/10.3390/ma14113034.

Finello, D., Marcus, H.L., 1979. Advances in and quantification of auger electron spectroscopy (AES). Electron and Positron Spectroscopies in Materials Science and Engineering. Elsevier, pp. 121–181. https://doi.org/10.1016/B978-0-12-139150-8.50010-5.

Galvão, E.S., Santos, J.M., Lima, A.T., Reis, N.C., Orlando, M.T.D.A., Stuetz, R.M., 2018. Trends in analytical techniques applied to particulate matter characterization: a critical review of fundaments and applications. Chemosphere 199, 546–568. https://doi.org/10.1016/j.chemosphere.2018.02.034.

Garrat-Reed, A.J., Bell, D.C., 2003. Energy Dispersive X-ray Analysis in the Electron Microscope, first ed. Garland Science, London. https://doi.org/10.4324/9780203483428.

Grenier, A., et al., 2017. Reaction heterogeneity in LiNi0.8Co0.15Al0.05O2 induced by surface layer. Chem. Mater. 29 (17), 7345–7352. https://doi.org/10.1021/acs.chemmater.7b02236.

Griffin, B.J., 2011. A comparison of conventional Everhart-Thornley style and in-lens secondary electron detectors-a further variable in scanning electron microscopy. Scanning 33 (3), 162–173. https://doi.org/10.1002/sca.20255.

Han, W., Zheng, M., Banerjee, A., Luo, Y.Z., Shen, L., Khursheed, A., 2020. Quantitative material analysis using secondary electron energy spectromicroscopy. Sci. Rep. 10 (1) https://doi.org/10.1038/s41598-020-78973-0.

Hashimoto, Y., Takeuchi, S., Sunaoshi, T., Yamazawa, Y., 2020. Voltage contrast imaging with energy filtered signal in a field-emission scanning electron microscope. Ultramicroscopy 209, 1–7. https://doi.org/10.1016/j.ultramic.2019.112889.

Heenan, T.M.M., et al., 2020. Resolving li-ion battery electrode particles using rapid lab-based X-ray nano-computed tomography for high-throughput quantification. Adv. Sci. 7 (12) https://doi.org/10.1002/advs.202000362.

Heon Kim, S., et al., 2014. Auger electron nanoscale mapping and x-ray photoelectron spectroscopy combined with gas cluster ion beam sputtering to study an organic bulk heterojunction. Appl. Phys. Lett. 104 (24) https://doi.org/10.1063/1.4885115.

Hodoroaba, V.D., Rades, S., Salge, T., Mielke, J., Ortel, E., Schmidt, R., 2016. Characterisation of nanoparticles by means of high-resolution SEM/EDS in transmission mode. IOP Conf. Ser. Mater. Sci. Eng. 109 (1) https://doi.org/10.1088/1757-899X/109/1/012006.

Hofmann, S., 1992. Charging and charge compensation in AES analysis of insulators. J. Electron Spectrosc. Relat. Phenom. 59, 15–32.

Hupfeld, T., et al., 2018. A new approach to coat PA12 powders with laser-generated nanoparticles for selective laser sintering. Procedia CIRP 74, 244–248. https://doi.org/10.1016/j.procir.2018.08.103.

Hussain, A., et al., 2020. Theoretical calculations of the mean escape depth of secondary electron emission from compound semiconductor materials. J. Appl. Phys. 127 (12) https://doi.org/10.1063/1.5144721.

International Organisation for Standardisation, "ISO 18115–1:2013, Surface Chemical Analysis - Vocabulary," 2013.

Isaacs, M.A., et al., 2021. Advanced XPS characterization: XPS-based multi-technique analyses for comprehensive understanding of functional materials. Mater. Chem. Front. 5 (22), 7931–7963. https://doi.org/10.1039/d1qm00969a.

Ishida, N., Fukumitsu, H., Kimura, H., Fujita, D., 2014. Direct mapping of Li distribution in electrochemically lithiated graphite anodes using scanning Auger electron microscopy. J. Power Sources 248, 1118–1122. https://doi.org/10.1016/j.jpowsour.2013.09.121.

Jansson, A., Pejryd, L., 2016. Characterisation of carbon fibre-reinforced polyamide manufactured by selective laser sintering. Addit. Manuf. 9, 7–13. https://doi.org/10.1016/j.addma.2015.12.003.

Jbara, O., Belhaj, M., Odof, S., Msellak, K., Rau, E.I., Andrianov, M. v, 2001. Surface potential measurements of electron-irradiated insulators using backscattered and secondary electron spectra from an electrostatic toroidal spectrometer adapted for scanning electron microscope applications. Rev. Sci. Instrum. 72 (3), 1788–1795. https://doi.org/10.1063/1.1344596.

Jepson, M.A.E., Khan, K., Hayward, T.J., Inkson, B.J., Rodenburg, C., 2010. The effect of oxidation and carbon contamination on SEM dopant contrast. J. Phys. Conf. Ser. 241 (1) https://doi.org/10.1088/1742-6596/241/1/012078.

Joy, D.C., Joy, C.S., 1996. Low voltage scanning electron microscopy. Micron 27 (3–4), 247–263. https://doi.org/10.1016/0968-4328(96)00023-6.

Joy, D.C., Prasad, M.S., Meyer, H.M., 2004. Experimental secondary electron spectra under SEM conditions. J. Microsc. 215 (1), 77–85. https://doi.org/10.1111/j.0022-2720.2004.01345.x.

Jun, D.W., Yoon, C.S., Kim, U.H., Sun, Y.K., 2017. High-energy density core-shell structured Li[Ni0.95Co0.025Mn0.025]O2 cathode for lithium-ion batteries. Chem. Mater. 29 (12), 5048–5052. https://doi.org/10.1021/acs.chemmater.7b01425.

Kazemian, P., Mentink, S.A.M., Rodenburg, C., Humphreys, C.J., 2007. Quantitative secondary electron energy filtering in a scanning electron microscope and its applications. Ultramicroscopy 107 (2–3), 140–150. https://doi.org/10.1016/j.ultramic.2006.06.003.

Khursheed, A., 2015. Energy analyzer attachments for the scanning electron microscope. Microsc. Microanal. 21 (S4), 130–135. https://doi.org/10.1017/S1431927615013264.

Khursheed, A., 2020. Secondary Electron Energy Spectroscopy in the Scanning Electron Microscope. World Scientific. https://doi.org/10.1142/12010.

Kienle, M., Plies, E., 2004. An off-axis multi-channel analyzer for secondary electrons. Nucl. Instrum. Methods Phys. Res., Sect. A: Accel., Spectrometers, Detect. Assoc. Equip. 519 (1–2), 325–330. https://doi.org/10.1016/j.nima.2003.11.170.

Kim, J., Park, H., 2021. Enhanced mass transfer in nanofluid electrolytes for aqueous flow batteries: the mechanism of nanoparticles as catalysts for redox reactions. J. Energy Storage 38. https://doi.org/10.1016/j.est.2021.102529.

Kim, J., Lee, H., Cha, H., Yoon, M., Park, M., Cho, J., 2018. Prospect and reality of Ni-rich cathode for commercialization. Adv. Energy Mater. 8 (6), 1702028–1702053. https://doi.org/10.1002/aenm.201702028.

Konvalina, I., Mika, F., Krátký, S., Materna Mikmeková, E., Müllerová, I., 2019. In-lens band-pass filter for secondary electrons in ultrahigh resolution SEM. Materials 12 (14), 2307. https://doi.org/10.3390/ma12142307.

Kumar, V., et al., 2017. Nanoscale mapping of bromide segregation on the cross sections of complex hybrid perovskite photovoltaic films using secondary electron hyperspectral imaging in a scanning electron microscope. ACS Omega 2 (5), 2126–2133. https://doi.org/10.1021/acsomega.7b00265.

Kumar, V., et al., 2018. Stoichiometry-dependent local instability in MAPbI3 perovskite materials and devices. J. Mater. Chem. A 6 (46), 23578–23586. https://doi.org/10.1039/c8ta08231f.

Leung, C.L.A., Marussi, S., Towrie, M., Atwood, R.C., Withers, P.J., Lee, P.D., 2019. The effect of powder oxidation on defect formation in laser additive manufacturing. Acta Mater. 166, 294–305. https://doi.org/10.1016/j.actamat.2018.12.027.

Li, C., et al., 2018. A Monte Carlo modeling on charging effect for structures with arbitrary geometries. J. Phys. D: Appl. Phys. 51 (16) https://doi.org/10.1088/1361-6463/aab2cf.

Li, C., Da, B., Ding, Z.J., 2020. Monte Carlo study on the surface potential measurement using the peak-shift method. Appl. Surf. Sci. 504 https://doi.org/10.1016/j.apsusc.2019.144138.

Liao, J.-Y., Oh, S.-M., Manthiram, A., 2016. Core/double-shell type gradient Ni-Rich LiNi 0.76 Co 0.10 Mn 0.14 O 2 with high capacity and long cycle life for lithium-ion batteries. Appl. Mat. Interfaces 8, 24543–24549. https://doi.org/10.1021/acsami.6b06172.

Liberman, L., Kleinerman, O., Davidovich, I., Talmon, Y., 2020. Micrograph contrast in low-voltage SEM and cryo-SEM. Ultramicroscopy 218. https://doi.org/10.1016/j.ultramic.2020.113085.

Lim, J.-M., et al., 2020. Enhancing nanostructured nickel-rich lithium-ion battery cathodes via surface stabilization. J. Vac. Sci. Technol. A 38 (6), 063210. https://doi.org/10.1116/6.0000580.

Lin, Y., Joy, D.C., 2005. A new examination of secondary electron yield data. Surf. Interface Anal. 37 (11), 895–900. https://doi.org/10.1002/sia.2107.

Llovet, X., Moy, A., Pinard, P.T., Fournelle, J.H., 2021. Electron probe microanalysis: a review of recent developments and applications in materials science and engineering. Prog. Mater. Sci. 116 https://doi.org/10.1016/j.pmatsci.2020.100673.

Lorusso, G.F., et al., 2017. Enabling CD SEM metrology for 5nm technology node and beyond. Metrol., Insp., Process Control Microlithogr. XXXI 10145, 1–9. https://doi.org/10.1117/12.2257468.

Lu, D., et al., 2021. Secondary electron-, Auger electron- and reflected electron-spectroscopy study on sp2-hybridization carbon materials: HOPG, carbon glass and carbon fiber. J. Electron Spectrosc. Relat. Phenom. 250 https://doi.org/10.1016/j.elspec.2021.147086.

Masters, R.C., et al., 2015. Sub-nanometre resolution imaging of polymer-fullerene photovoltaic blends using energy-filtered scanning electron microscopy. Nat. Commun. 6, 1–9. https://doi.org/10.1038/ncomms7928.

Masters, R.C., et al., 2019. Mapping polymer molecular order in the sem with secondary electron hyperspectral imaging. Adv. Sci. 6 (5) https://doi.org/10.1002/advs.201801752.

Michael, J.R., 2011. High resolution at low beam energy in the SEM: resolution measurement of a monochromated SEM. Scanning 33 (3), 147–154. https://doi.org/10.1002/sca.20254.

Mikmeková, E.M., et al., 2020. Low-energy electron microscopy of graphene outside UHV: electron-induced removal of PMMA residues used for graphene transfer. J. Electron Spectrosc. Relat. Phenom. 241 https://doi.org/10.1016/j.elspec.2019.06.005.

Murrieta-Pazos, I., Gaiani, C., Galet, L., Cuq, B., Desobry, S., Scher, J., 2011. Comparative study of particle structure evolution during water sorption: Skim and whole milk powders. Colloids Surf. B: Biointerfaces 87 (1), 1–10. https://doi.org/10.1016/j.colsurfb.2011.05.001.

Nagoshi, M., Sato, K., Aoyama, T., 2017. Low-voltage scanning electron microscopy as a tool for surface imaging and analysis of practical materials. J. Surf. Anal. 24 (2), 129–135.

Niculae, A., et al., 2012. Optimizing the low energy performance of pole-shoe EDX detectors. Microsc. Microanal. 18, 1202–1203. https://doi.org/10.1017/S1431927612007866.

Nohl, J.F., 2020. Secondary electron hyperspectral imaging: nanostructure and chemical analysis for the LV-SEM. Mat. Sci. Technol. 36 (5), 527–539. https://doi.org/10.1080/02670836.2020.1732609.

Ogi, T., Modesto-Lopez, L.B., Iskandar, F., Okuyama, K., 2007. Fabrication of a large area monolayer of silica particles on a sapphire substrate by a spin coating method. Colloids Surf. A: Physicochem. Eng. Asp. 297 (1–3), 71–78. https://doi.org/10.1016/j.colsurfa.2006.10.027.

Oxford Instruments, "Ultim ® Extreme Silicon Drift Detector: Delivering solutions beyond conventional nano-analysis in the SEM EDS 1 µm," 2019.

Pawley, J.B., 2007. In: Schatten, H., Pawley, J.B. (Eds.), Biological Low-Voltage Scanning Electron Microscopy, first ed. Springer, New York.

Pinard, P.T., Burgess, S., Zhang, J.Q., Holland, J., Statham, P., 2018. X-ray microanalysis at high count rate with latest generation silicon drift energy dispersive spectrometer. Microsc. Microanal. 24 (S1), 724–725. https://doi.org/10.1017/s1431927618004117.

Piňos, J., Mikmeková, Š., Frank, L., 2017. About the information depth of backscattered electron imaging. J. Microsc. 266 (3), 335–342. https://doi.org/10.1111/jmi.12542.

Polak, M.P., Morgan, D., 2021. MAST-SEY: material simulation toolkit for secondary electron yield. A monte carlo approach to secondary electron emission based on complex dielectric functions. Comput. Mater. Sci. 193 https://doi.org/10.1016/j.commatsci.2021.110281.

M.T. Postek and A.E. Vladár, Does your SEM really tell the truth? How would you know? Part 4: Charging and its mitigation, in Scanning Microscopies 2015, Oct. 2015, vol. 9636, p. 963605. doi: ⟨10.1117/12.2195344⟩.

Prasad, M.S., Joy, D.C., 2003. Measurements of absolute X-ray generation efficiency for selected K, L, and M-Lines. Scanning 25, 210–215. ⟨http://pciserver.bio.utk.edu/metrology⟩.

Rades, S., et al., 2014. High-resolution imaging with SEM/T-SEM, EDX and SAM as a combined methodical approach for morphological and elemental analyses of single engineered nanoparticles. RSC Adv. 4 (91), 49577–49587. https://doi.org/10.1039/c4ra05092d.

Rasch, R., Stricher, A., Truss, R.W., 2014. Energy filtered low voltage 'in lens detector' SEM and XPS of natural fiber surfaces. J. Appl. Polym. Sci. 131 (9) https://doi.org/10.1002/app.39572.

Reimer, L., 1998. Scanning Electron Microscopy: Physics of Image Formation and Microanalysis, second ed. Springer, Berlin, London. https://doi.org/10.1007/978-3-7091-6679-6_3.

Ro, C., Linton, R.W., 1992. Characterization of LiF Using XPS. Surf. Sci. Spectra 1 (3), 277–283. https://doi.org/10.1116/1.1247651.

Roberts, R.H., el Gomati, M.M., Kudjoe, J., Barkshire, I.R., Bean, S.J., Prutton, M., 1997. Measurement science and technology a miniature, all-electrostatic, field emission electron column for surface analytical microscopy. Meas. Sci. Technol. 8, 536–545.

Rodenburg, C., Jepson, M.A.E., Inkson, B.J., Bosch, E.G.T., Humphreys, C.J., 2010. Energy filtered scanning electron microscopy: applications to characterisation of semiconductors. J. Phys. Conf. Ser. 241 (1) https://doi.org/10.1088/1742-6596/241/1/012074.

Rodenburg, C., Jepson, M.A.E., Inkson, B.J., Bosch, E., Chee, A.K.W., Humphreys, C.J., 2010. Energy filtered scanning electron microscopy: applications to dopant contrast. J. Phys.: Conf. Ser. 209 https://doi.org/10.1088/1742-6596/209/1/012053.

Rodenburg, C., Jepson, M.A.E., Bosch, E.G.T., Dapor, M., 2010. Energy selective scanning electron microscopy to reduce the effect of contamination layers on scanning electron microscope dopant mapping. Ultramicroscopy 110 (9), 1185–1191. https://doi.org/10.1016/j.ultramic.2010.04.008.

Salehi, A., Pircheraghi, G., 2021. Thermo-oxidative degradation during sintering of polyethylene particles. J. Appl. Polym. Sci. 138 (19) https://doi.org/10.1002/app.50373.

Salvi, A.M., Castle, J.E., Watts, J.F., Desimoni, E., 1995. Peak fitting of the chromium 2p XPS spectrum. Appl. Surf. Sci. 90, 333–341.

J. Schafer, R. Schoppe, J. Holzl, and R. Feder, Experimental and theoretical study of the Angular Resolved Secondary Electron Spectroscopy (ARSES) for W(100) in the energy range $0 < E < 20$ eV 1981.

U. Scheithauer, Experimental setups for XPS measurements beyond the instrumental lateral resolution limit, in *Surface and Interface Analysis*, Dec. 2020, vol. 52, no. 12, pp. 1185–1190. doi: ⟨10.1002/sia.6828⟩.

Scheithauer, U., 2008. Quantitative lateral resolution of a Quantum 2000 X-ray microprobe. Surf. Interface Anal. 40 (3–4), 706–709. https://doi.org/10.1002/sia.2662.

Schoning, A., Lackner, R., Bechteler, A., Liebel, A., Niculae, A., Soltau, H., 2017. A compact high solid angle EDX detector system for SEM and TEM. Microsc. Microanal. 23 (S1), 76–77. https://doi.org/10.1017/s1431927617001064.

Schönjahn, C., Humphreys, C.J., Glick, M., 2002. Energy-filtered imaging in a field-emission scanning electron microscope for dopant mapping in semiconductors. J. Appl. Phys. 92 (12), 7667–7671. https://doi.org/10.1063/1.1525862.

Seah, M.P., 1969. Slow electron scattering from metals I. The emission of true secondary electrons. Surf. Sci. 17.

Seiler, H., 1983. Secondary electron emission in the scanning electron microscope. J. Appl. Phys. 54 (11) https://doi.org/10.1063/1.332840.

Seong, W.M., Kim, Y., Manthiram, A., 2020. Impact of residual lithium on the adoption of high-nickel layered oxide cathodes for lithium-ion batteries. Chem. Mater. 32 (22), 9479–9489. https://doi.org/10.1021/acs.chemmater.0c02808.

D. Shemesh, A. Boehm, O. Greenberg, K. Dotan, "Advanced elemental analysis methods for sub 30nm defects in a defect review SEM," 2011. doi: ⟨10.1109/ASMC.2011.5898179⟩.

Small, J.A., 2002. The analysis of particles at low accelerating voltages (≤ 10 kV) with energy dispersive x-ray spectroscopy (EDS. J. Res. Natl. Inst. Stand. Technol. 107 (6), 555–566. https://doi.org/10.6028/jres.107.047.

Srinivasan, A., Han, W., Zheng, M., Khursheed, A., 2021. Characterization of materials using the secondary electron energy spectromicroscopy technique. Opt. Mater.: X 12. https://doi.org/10.1016/j.omx.2021.100121.

Stehling, N., et al., 2018. New perspectives on nano-engineering by secondary electron spectroscopy in the helium ion and scanning electron microscope. MRS Commun. 8 (2), 226–240. https://doi.org/10.1557/mrc.2018.75.

Stehling, N.A., 2020. Scanning Electron Microscopy for Nano-morphology Characterisation of Complex Hierarchical Polymer Structures. University of Sheffield, pp. 1–172.

Stevie, F.A., Donley, C.L., 2020. Introduction to x-ray photoelectron spectroscopy. J. Vac. Sci. Technol. A 38 (6), 063204. https://doi.org/10.1116/6.0000412.

Takeichi, Y., Goto, K., Gaidarova, V., 1996. True Auger spectral shapes (standards). Appl. Surf. Sci. 100, 25–29.

Tammas-Williams, S., Withers, P.J., Todd, I., Prangnell, P.B., 2017. The influence of porosity on fatigue crack initiation in additively manufactured titanium components. Sci. Rep. 7 (1) https://doi.org/10.1038/s41598-017-06504-5.

S. Tougaard, "Accuracy of the Non-destructive Surface Nanostructure Quantification Technique Based on Analysis of the XPS or AES Peak Shape," 1998.

Tsosie, H., Thomas, J., Strong, J., Zavaliangos, A., 2017. Scanning electron microscope observations of powder sticking on punches during a limited number ($N < 5$) of compactions of acetylsalicylic acid. Pharm. Res. 34 (10), 2012–2024. https://doi.org/10.1007/s11095-017-2186-3.

Tsutsumi, K., Shima, M., Tanaka, A., 2014. Advanced analysis of active materials in li-ion battery by XPS and AES. JEOL N. 49 (1), 59–72. ⟨http://scholar.google.com⟩.

Vladár, A.E., Postek, M.T., 2005. Electron beam-induced sample contamination in the SEM. Microsc. Microanal. 11, 764–765. https://doi.org/10.1017/S1431927605507785.

Vladár, A.E., Postek, M.T., Ming, B., 2009. On the sub-nanometer resolution of scanning electron and helium ion microscopes. Microsc. Today 17 (2), 6–13. https://doi.org/10.1017/s1551929500054420.

Walde, C., Ristau, R., Cote, D., 2018. Automated 3D EBSD for metallic powders. MethodsX 5, 652–655. https://doi.org/10.1016/j.mex.2018.06.001.

Walker, C.G.H., El-Gomati, M.M., Assa'd, A.M.D., Zadražil, M., 2008. The secondary electron emission yield for 24 solid elements excited by primary electrons in the range 250-5000 ev: a theory/experiment comparison. Scanning 30 (5), 365–380. https://doi.org/10.1002/sca.20124.

Watts, J.F., Wolstenholme, J., 2003. An Introduction to Surface Analysis by XPS and AES. John Wiley & Sons, Ltd, Chichester, UK. https://doi.org/10.1002/0470867930.

R.D. Willis, F.T. Blanchard, T.L. Conner, C. Morris, "Guidelines for the Application of SEM/EDX Analytical Techniques to Particulate Matter Samples," 2002.

Willis, R.F., Christensen, N.E., 1978. Secondary-electron-emission spectroscopy of tungsten: angular dependence and phenomenology. Phys. Rev. 8 (10), 5141–5161.

Willis, R.F., Fitton, B., 1972. The band structure of graphite studied by secondary electron emission. J. Vac. Sci. Technol. 9 (2), 651–656. https://doi.org/10.1116/1.1317746.

Willis, R.F., Fitton, B., Skinner, D.K., 1972. Study of carbon-fiber surfaces using Auger and secondary electron emission spectroscopy. J. Appl. Phys. 43 (11), 4412–4419. https://doi.org/10.1063/1.1660936.

Wolff, P.A., 1954. Theory of secondary electron cascade in metals. Phys. Rev. B. 95 (1), 56–66.

Wood, K.N., Teeter, G., 2018. XPS on li-battery-related compounds: analysis of inorganic SEI phases and a methodology for charge correction. ACS Appl. Energy Mater. 1 (9), 4493–4504. https://doi.org/10.1021/acsaem.8b00406.

Woodruff, D.P., 2016. Modern Techniques of Surface Science, third ed. Cambridge University Press.

Wuhrer, R., Moran, K., 2016. Low voltage imaging and X-ray microanalysis in the SEM: challenges and opportunities. OP Conference Series: Materials Science and Engineering 109 (1). https://doi.org/10.1088/1757-899X/109/1/012019.

Xing, Q., 2016. Information or resolution: Which is required from an SEM to study bulk inorganic materials? Scanning 38 (6), 864–879. https://doi.org/10.1002/sca.21336.

Xu, X., et al., 2019. Progressive concentration gradient nickel-rich oxide cathode material for high-energy and long-life lithium-ion batteries. J. Mat. Chem. A 7, 7728–7735. https://doi.org/10.1039/c9ta00224c.

Yamamoto, Y., et al., 2016. The study of 'window-less' EDS detector with low voltage FE-SEM. Microsc. Microanal. 22 (S3), 640–641. https://doi.org/10.1017/s1431927616004050.

Yan, C., Hao, L., Xu, L., Shi, Y., 2011. Preparation, characterisation and processing of carbon fibre/polyamide-12 composites for selective laser sintering. Compos. Sci. Technol. 71 (16), 1834–1841. https://doi.org/10.1016/j.compscitech.2011.08.013.

Yan, P., et al., 2018. Tailoring grain boundary structures and chemistry of Ni-rich layered cathodes for enhanced cycle stability of lithium-ion batteries. Nat. Energy 3 (7), 600–605. https://doi.org/10.1038/s41560-018-0191-3.

Young, R., et al., 2008. Extreme high-resolution SEM: a paradigm shift. Microsc. Today 16 (4), 24–29. https://doi.org/10.1017/s1551929500059745.

Zarraoa, L., González, M.U., Paulo, Á.S., 2019. Imaging low-dimensional nanostructures by very low voltage scanning electron microscopy: ultra-shallow topography and depth-tunable material contrast. Sci. Rep. 9 (1) https://doi.org/10.1038/s41598-019-52690-9.

Zhu, W., et al., 2019. Ultrathin Al2O3 coating on LiNi0.8Co0.1Mn0.1O2 cathode material for enhanced cycleability at extended voltage ranges. Coatings 9 (2). https://doi.org/10.3390/COATINGS9020092.

Zou, Y.B., Mao, S.F., Da, B., Ding, Z.J., 2016. Surface sensitivity of secondary electrons emitted from amorphous solids: calculation of mean escape depth by a Monte Carlo method. J. Appl. Phys. 120 (23) https://doi.org/10.1063/1.4972196.